MULTI-SCALE MODELING OF AGING OF WASPALOY SUPERALLOY: PREDICTION OF MICROSTRUCTURE EVOLUTION AND COUPLING WITH MECHANICAL PROPERTIES

A THESIS SUBMITTED TO
THE GRADUATE SCHOOL OF NATURAL AND APPLIED SCIENCES
OF
MIDDLE EAST TECHNICAL UNIVERSITY

BY

BETÜL GÖVERCİN

IN PARTIAL FULFILLMENT OF THE REQUIREMENTS
FOR
THE DEGREE OF MASTER OF SCIENCE
IN
METALLURGICAL AND MATERIALS ENGINEERING

JANUARY 2024

Approval of the thesis:

MULTI-SCALE MODELING OF AGING OF WASPALOY SUPERALLOY: PREDICTION OF MICROSTRUCTURE EVOLUTION AND COUPLING WITH MECHANICAL PROPERTIES

submitted by **BETÜL GÖVERCİN** in partial fulfillment of the requirements for the degree of **Master of Science** i**n Metallurgical and Materials Engineering, Middle East Technical University** by,

Prof. Dr. Halil Kalıpçılar
Dean, **Graduate School of Natural and Applied Sciences** _____

Prof. Dr. Ali Kalkanlı
Head of the Department, **Metallurgical and Materials Eng.** _____

Assoc. Prof. Dr. Caner Şimşir
Supervisor, **Metallurgical and Materials Eng., METU** _____

Assist. Prof. Dr. Eda Aydoğan Güngör
Co-Supervisor, **Metallurgical and Materials Eng., METU** _____

Examining Committee Members:

Prof. Dr. C. Hakan Gür
Metallurgical and Materials Eng., METU _____

Assoc. Prof. Dr. Caner Şimşir
Metallurgical and Materials Eng., METU _____

Assist. Prof. Dr. Eda Aydoğan Güngör
Metallurgical and Materials Eng., METU _____

Assoc. Prof. Dr. Volkan Kılıçlı
Metallurgical and Materials Eng., Gazi Uni. _____

Assoc. Prof. Dr. Metehan Erdoğan
Metallurgical and Materials Eng., AYBÜ _____

Date: 17.01.2024

I hereby declare that all information in this document has been obtained and presented in accordance with academic rules and ethical conduct. I also declare that, as required by these rules and conduct, I have fully cited and referenced all material and results that are not original to this work.

Name Last name: Betül Gövercin

Signature:

ABSTRACT

MULTI-SCALE MODELING OF AGING OF WASPALOY SUPERALLOY: PREDICTION OF MICROSTRUCTURE EVOLUTION AND COUPLING WITH MECHANICAL PROPERTIES

Gövercin, Betül
Master of Science, Metallurgical and Materials Engineering
Supervisor: Assoc. Prof. Dr. Caner Şimşir
Co-Supervisor: Assist. Prof. Dr. Eda Aydoğan Güngör

January 2024, 116 pages

Ni-based superalloys operating under high temperatures, ensuing compression and tension type of loads, and highly corrosive environment are mostly used in tubine engines. In order to provide high temperature strength needed for operational conditions, heat treatment processes are crucial for those materials. Therefore, modelling of processes according to required microstructure and properties have a great importance for aerospace and power plant industries to reduce the number of time-consuming and highly costing manufacturing operations.

In this study, effect of heat treatment on Waspaloy is investigated starting from solidification to implementation on mechanical properties. Solidification modelling is constituted with CALPHAD method by using PANDAT. Offered and applied heat treatment process is designed by using thermodynamic and kinetic models and the results are compared with SEM, TEM and EDS outcomes. Model results are used for yield strength estimation comprising precipitation, solid solution, Orowan, coherency and grain size hardening at varying temperatures. Aged specimens are

subjected to tensile tests at room temperature, 580°C, 650°C, 720°C and 1100°C with Gleeble 3500 system.

The generic approach applied in this study has given that the modelled heat treatment and experimental study are both shown ɣ' precipitate sizes with approximately 25 nm. Yield strength estimation constructed with the modelling results has shown 1-8 percent variation from the experimental results at room and elevated temperatures whereas in 1100°C condition, predictions differed greatly. Therefore, it is declared that this model can predict the yield strength of the material but needs further developments to predict all conditions accurately.

Keywords: Waspaloy, Ni-based superalloy, heat treatment, PANDAT, modelling

ÖZ

WASPALOY SÜPER ALAŞIMININ YAŞLANDIRMASININ ÇOK ÖLÇEKLİ MODELLEMESİ: MİKROYAPININ DEĞİŞİMİ VE MEKANİK ÖZELLİKLERLE BAĞDAŞTIRILMASI

Gövercin, Betül
Yüksek Lisans, Metalurji ve Malzeme Mühendisliği
Tez Yöneticisi: Doç. Dr. Caner Şimşir
Ortak Tez Yöneticisi: Dr. Öğr. Üyesi Eda Aydoğan Güngör

Ocak 2024, 116 sayfa

Yüksek sıcaklıklarda, basma ve çekme tipi yükler altında ve aşırı korozif ortamlarda çalışabilen Nikel bazlı süper alaşımlar çoğunlukla türbin motorlarında kullanılmaktadır. Çalışma koşullarının gerektirdiği yüksek sıcaklık dayanımını sağlamak için bu malzemelerde ısıl işlem prosesleri büyük önem taşımaktadır. Bu nedenle, süreçlerin gerekli mikro yapı ve özelliklere göre modellenmesi, havacılık ve enerji santralleri endüstrileri için zaman alıcı ve yüksek maliyetli üretim operasyonlarının azaltılması açısından büyük önem taşımaktadır.

Bu çalışmada Waspaloy'a uygulanan ısıl işlemin katılaşma aşamasından başlayarak mekanik özelliklere kadar olan etkisi araştırılmıştır. Katılaşma modellemesi PANDAT kullanılarak CALPHAD yöntemiyle oluşturulmuştur. Sunulan ve uygulanan ısıl işlem prosesi, termodinamik ve kinetik modeller kullanılarak tasarlanmış ve sonuçlar SEM, TEM ve EDS sonuçlarıyla karşılaştırılmıştır. Model sonuçları, çökeltme, katı çözelti, Orowan, kafes uygunsuzluğu ve tane boyutu sertleşmesini içeren akma dayanımı tahmini için kullanılmıştır. Yaşlandırılmış numuneler oda sıcaklığında, 580°C, 650°C, 720°C ve 1100°C'de Gleeble 3500 sistemi ile çekme testlerine tabi tutulmuştur.

Bu çalışmada uygulanan çerçeveli yaklaşım, modellenen ısıl işlem ve deneysel çalışmanın her ikisinde de yaklaşık 25 nm'lik ɣ' çökelti boyutlarının elde edildiğini göstermiştir. Modelleme sonuçlarıyla oluşturulan akma dayanımı tahmini, oda sıcaklığında ve yüksek sıcaklıklarda deneysel sonuçlardan yüzde 1-8 oranında farklılık gösterirken, 1100°C koşulunda tahminler büyük ölçüde farklılık göstermiştir. Dolayısıyla bu modelin, malzemenin akma dayanımını tahmin edebildiği ancak tüm koşulları doğru bir şekilde tahmin edebilmek için geliştirilmesi gerektiği görülmüştür.

Anahtar Kelimeler: Waspaloy, Nikel bazlı süperalaşım, ısıl işlem, PANDAT, modelleme

To my beloved family

ACKNOWLEDGMENTS

I would like to express my gratitude to Assoc. Prof. Dr. Caner Şimşir and Assist. Prof. Dr. Eda Aydoğan Güngör for their guidance, advice, criticism, and encouragement through all.

This thesis could not be completed without the help of Fatih Kalıp Makine San., ERDEMİR, Lukasiewicz Research Network – Institute for Ferrous Metallurgy, CompuTherm and PANDAT companies. I would also like to thank Ömer Şahin, Özgür Duygulu and Rasim Köksal Ertan for their greatest contributions to this study.

My heartiest thanks to my friends who were always there with endless support, encouragement, and their belief.

My deepest gratitude is for my parents for all their support which encouraged me for many achievements my entire life, their endless belief and love.

TABLE OF CONTENTS

LIST OF TABLES

TABLES

LIST OF FIGURES

FIGURES

ABBREVIATIONS

LIST OF ABBREVIATIONS

EDS	Energy Dispersive Spectroscopy
FCC	Face Centered Cubic
SEM	Scanning Electron Microscopy
VIM	Vacuum Induction Melting
VAR	Vacuum Arc Remelting
ESR	Electro-Slag Refining
SEM	Scanning Electron Microscope
TEM	Transmission Electron Microscopy
OES	Optic Emission Spectroscopy
EDS	Energy Dispersive Spectroscopy
XRD	X-Ray Diffraction

SYMBOLS

LIST OF SYMBOLS

ɣ	Gamma
ɣ'	Gamma Prime
T	Temperature
β_i	Solid Solution Constant
x_i	Atomic Fraction
σ_0	Lattice Strength
σ_{gh}	Grain Boundary Strengthening
σ_{ph}	Precipitation Strengthening
σ_{ss}	Solid Solution Strengthening
σ_{oro}	Orowan Strengthening
σ_{coh}	Coherency Strengthening
k_y	Hall-Petch Constant for Grain Boundary
M	Taylor's Factor
f	Gamma Prime Volume Fraction
b	Burgers Vector
γ_{APB}	Anti-Phase Boundary Energy
G	Shear Modulus
λ	Inter-Particle Distance

CHAPTER 1

THEORY and BACKGROUND

1.1 General

History of the superalloys starts with the increasing need of human's developing technology depending on more efficient systems. George B. Brayton worked on a cycle proving that the higher inlet temperatures of thermal systems resulting with increased effiency and called it Brayton cycle in 1872. This cycle is also known as Joule cycle and it was developed for higher efficient systems[1-3]. Later on with the increasing need for new energy resources, this theory led to the invention of steam turbines in 19^{th} century and continued with the development of gas turbines in the beginning of 1900s[4]. Nowadays, Brayton cycle is used in most of the jet engine designs. After these developments, it has been understood that high temperature operations result with higher energies but the type of materials used in those systems was a limitation for increasing operating temperatures.

As it has always been, wars are great periods to cultivate scientific researches to give countries an edge on one another and accelerate technological developments. In order to face with the increasing need on higher energy systems, especially in turbine engines and turbo superchargers, superalloys were developed in 1940s. These alloys showed superior mechanical properties that can be maintained to elevated temperatures leading to improved effiency in those systems with less fuel burned. The idea of "developing alloys that can withstand higher temperatures where less fuel is used" has always been the main goal for developing more efficient engines. Consequently, development of superalloys and their manufacturing processes became a more important subject over the years [5].

Superalloys worked under extreme operating conditions such as high temperatures, severe corrosion, and high mechanical loads. These requirements can be explained as:

1. **High Temperature Material**

   To classify an alloy as a "high temperature material", the material must be appropriate for operating at temperatures close to its melting point and have the ability to withstand loading at these temperatures. The "high temperature" term is used for temperatures where the operating temperature to melting temperature ratio is 0.6 or higher.

2. **Mechanical Degradation**

   These materials operate under varying mechanical loads at high temperatures where a substantial resistance to mechanical degradation is expected for long durations. The creep performance of these materials is a key factor for the design of turbine systems where the creep is a time-dependent, inelastic, and irrecoverable deformation that drives on with thermally activated processes at high temperatures. Materials used in structural parts are also expected to maintain static properties such as high yield strength, ultimate tensile strength, and fracture toughness at severe conditions.

3. **Corrosive Environment**

   Fuels used in these engines expose high levels of sulfur and potassium salt when they are burned; and at high operating temperatures, with the increasing possibility of oxidation of the part interacting with these drains, surface degradation followed by the failure of the component occurs. For marine engines, seawater also accelerates corrosion and lowers the component life where the design of these materials and further processes become more important for efficient and appropriate material use.

Considering all these requirements, superalloys have been developed based on Fe, Ni, and Co with alloying Cr, W, Mo, Ta, Ti, Al, and Nb. Iron-based superalloys have been developed from austenitic stainless steel with a FCC crystal system where Ni is used as a stabilizer for the matrix for nickel-iron-cobalt-based superalloys. These alloys gain their strength from solid solution strengthening of alloying elements dissolved in matrix and precipitation hardening with Ni_3Al (γ'), Ni_3Nb (γ''), and Ni_3Ti (η) precipitates [6-7].

Cobalt-based superalloys attain their strength from solid solution strengthening and carbides formed in the grains and grain boundaries. As related to the alloying elements contributed to the solid solution hardening, Co-based alloys are known for their outstanding corrosion resistance, thermal fatigue resistance, and weldability. On the other hand, these alloys have lower strength, ductility, and fracture toughness properties which makes them inappropriate to use in jet engines, unlike Ni-based alloys.

There were many other investigated materials: titanium alloys have poor oxidation resistance at elevated temperatures limiting the operating temperature to around 700°C, SiC and SiN ceramics have excellent oxidation and creep resistance but very poor toughness and ductility where cycling loading in turbines occurring, high strength creep resistant ferritic steels cannot operate up to 700°C even though they offer low cost, and Zirconia-based ceramics are limited to use only as thermal barrier coating. Ni-based superalloys are the widest group that introduces varying needs.

Ni-based superalloys have a highly stable FCC matrix and can be strengthened mainly with precipitation hardening, solid solution hardening, Orowan strengthening, grain boundary strengthening, and many other mechanisms. These alloys have high thermomechanical strength, surface stability, oxidation, and corrosion resistance due to the Cr, Al, Ti, and Nb used in alloying.

A turbine engine has different sections that undergo varying operational needs. In order to select the material appropriately for those parts, it is important to understand those sections. As can be seen in the figure below, a turbine mainly consists of 5 sections: compressor, shaft, combustion chamber, turbine, and exhaust nozzle.

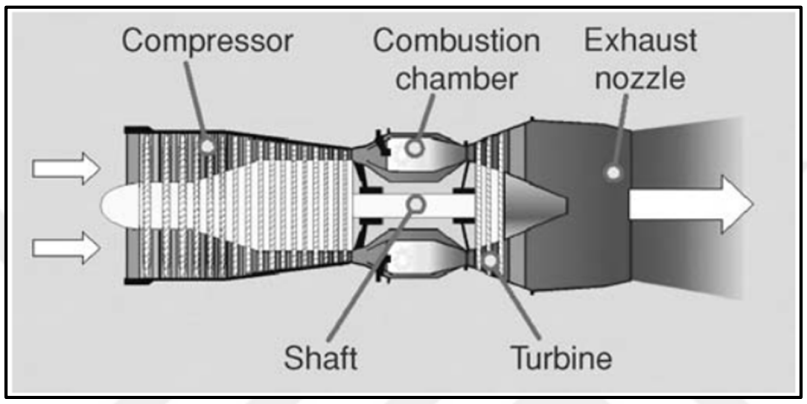

Figure 1-1 A basic illustration of a basic gas turbine engine [5].

In the compressor part, the aim is to increase the pressure of the incoming air by squeezing it with compressor blades and discs. In this part, since the temperature of entering air is quite low compared to the turbine part, the material choice for this section favors alloys that can withstand high mechanical loads but relatively low temperatures such as titanium and nickel alloys.

The pressurized air is mixed with fuel and ignited in the combustion chamber. In this section – depending on the fuel, pressure, and engine – temperatures can rise up to 2000°C. Therefore, the material selection must be done accordingly. For this part, the most commonly used materials are Ni-base superalloys with refractory materials and ceramic mixes.

In order to transmit the mechanical work that comes out after the combusted hot gases enter and expand in the turbine to drive the compressor, the shaft takes place to transfer the torque between the sections. For the shaft, mostly high-strength steels

such as 25Cr1Mo1VA, 30CrNi3Mo1VA, 26CrNi3Mo2VA, 23CrMoNiWV88, and X750 are used [8].

Materials used in such applications have high material and processing costs regarding the equipment, energy, and labor needed, making them inappropriate for many trial-error processes. These materials are designed to provide high-temperature capabilities for enhanced engine cycles as well as being as lightweight as possible for higher operational speeds and increased engine performance. In order to meet all these requirements together with high-temperature strength and corrosion resistance, reducing the number of trials for production and processing stages becomes an important issue. Consequently, material and process design gains prominence.

1.2 Nickel-Based Superalloys

Ni-based superalloys are the most complex superalloy group among the others as mentioned before since they are generally multiphase and multicomponent alloys with complicated microstructures. These alloys are mostly used in aero-engine applications as well as gas turbines for energy production. In the early 1900s, Ni-Cr alloys were developed and the effect of some elements such as Al and Ti have been investigated. The results show that Cr has given the alloy an excellent oxidation resistance and the Al-Ti partition showed a great increase in creep strength. Effects of some elements are summarized in the table below:

Table 1-1: Effect of elements in Nickel-based Superalloys [4]

Effect	**Element**
Solid Solution Strengthener	Co, Cr, Fe, Mo, W, Ta, Re
High Temperature Strength	Ni, Nb, C, Co, Mo, W
ɣ' former $Ni_3(Al, Ti)$	Al, Ti

Table 1-1 Cont'd.

Carbide Former	MC	Ta, Ti, Mo, Nb, Hf
	$M_{23}C_6$	Cr
	M_6C	Mo, W, Nb
	M_7C_3	Cr
Carbonitride M(CN)		C, N
Increasing ɣ' solvus temperature ve ɣ matrix melting point		Co
Second phase hardeners (precipitates) and/or intermetallics		Al, Ti, Nb
Oxidation Resistance		Ni, Al, Cr, Y, La, Ce, Si, Co, Mo
Hot Corrosion Resistance		La, Th
Sulfidation Resistance		Cr, Co, Si
Rupture Strength Improvement		B
Grain Boundary Refiner		B, C, Zr, Hf
Oxide Layer Adherence		Rare Earth Elements
Grain Boundary Segregation resulted Embrittlement		S, P, Si

Ni-based superalloys usually consist of at least 10 elements contributing to oxidation resistance, solid solution strengthening, ɣ' and ɣ" formation, and carbide formation. Besides the first and most important effect of these elements, they act as grain refiners, provide sulfidation resistance especially from the gases formed during combustion, improve high-temperature and rupture strength while can cause TCP phase formation, as well [5].

Superalloy properties are highly dependent on the type and amount of alloying elements. Ni-based superalloys generally consist of a high amount of Cr and Co for the oxidation and sulfidation resistance and these also take place in solid solution strengthening. Although a high percentage of Ni-based superalloys has precipitation hardening as their main strengthening mechanism, solid solution strengthening is also required for the applications where relatively lower strength values are enough and stable high-temperature properties are desired, especially at higher temperatures than ɣ' solvus. Al and Ti are main elements to form ɣ' phase where the precipitaion

hardening is dominating the strength of the material. Usually the sum of Al and Ti is found below 10 weight percentage in these superalloys. Nb is added when ɣ" phase is also needed in the microstructure. Fe, Mo, and W are also some of the elements that can be seen in most of Ni-based superalloys due to their contribution to solid solution strentghening and carbide formation; however, due to the high molar mass of W, new superalloy designs are focused on rare-earth element usage instead of tungsten to reduce the part weight for more fuel-efficient systems. B is also added to these alloys in very low amounts for the boride formation in order to ease the processing and have grain refining effect leading to more homogeneous microstructures [9].

Although the variation in chemical composition has an enormous effect on the properties of the material, production and processing methods have also changed through the history of Ni-based superalloys especially for higher thermomechanical properties by reducing the void formation, micro- and macro-segregation, providing a homogeneous microstructure with the grains & precipitates, and lastly, producing directional structures to increase the ductility of the material while keeping the strength of the part [10].

As can be seen in Figure 1-2, the use of superalloys has started with wrought alloys such as Waspaloy and MarM200, and continued with conventional casting, directional solidification, and finally the single crystal production. The aim in all these inventions mainly lies in the need for higher temperature materials and better mechanical properties. Because of the increasing demand in aviation over the years, many methods have been developed and many Ni-based superalloys have been introduced by companies. Cast and wrought alloys were the first groups and IN718, Waspaloy, Udimet720 are well-known materials in this group. There are possible casting methods such as VIM followed by VAR, VIM followed by ESR, or more controlled materials that undergone VIM, ESR and VAR for higher purity requirements. Since the casting microstructure is not applicable for operation under severe conditions, the alloys also undergo a hot forging application and further

process designs are done by accepting the initial microstructure obtained after cast and wrought processes.

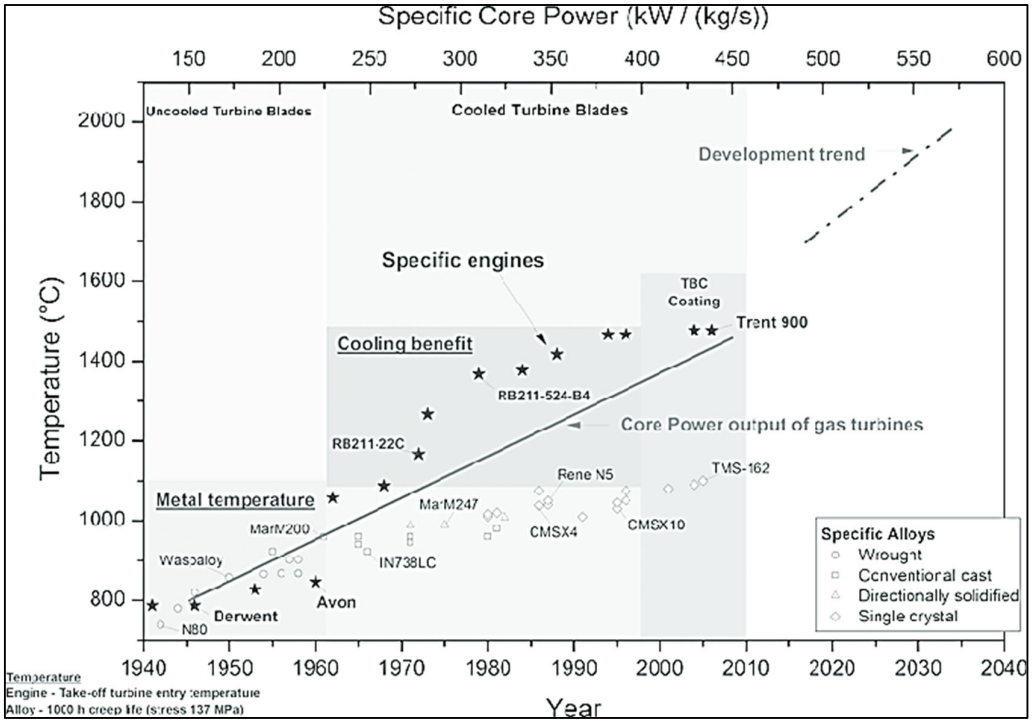

Figure 1-2 Evolution of Ni-based Superalloys over 70-years.

In order to increase the ductility and improve the creep strength, directional solidification methods have been used to produce these alloys and commercial products have taken place in the 1970s. This method is especially used for turbine blades where the columnar grains are aligned to the blade axis and dislocation climb length has been improved to resist higher stress values in this direction. With the success of directionally solidified polycrystalline materials, single crystal alloy production has taken the attention to eliminate the grain boundaries (that can cause some defects such as vacancy formations and grain boundary sliding) and reach

higher strengths without using the grain boundary strengtheners[11-15]. Nowadays, 6th generation single crystal superalloys are used in some parts of the engines.

1.2.1 Phases in Ni-based Superalloys

Ni-based superalloys consist of many alloying elements, leading to multiphase formation in the materials and increasing the system complexity. Ni-based superalloys are composed of ɣ matrix, ɣ' and ɣ" precipitates, carbides, borides, and TCP phases [16].

1.2.1.1 ɣ (Gamma) Matrix

Nickel is known with its stable FCC crystal structure allowing the deformation of the material due to the high dislocation motion in the structure from room temperature up to 1455°C. The continuous ɣ matrix has FCC structure due to the Ni, and the solid solution elements such as Co, Cr, Fe, Mo, and W takes place within this structure. These elements, with the similar atomic radii to Ni, partition to the austenitic ɣ phase, and stabilize it through the operational conditions [5]. Solid solution strengthened ɣ matrix shows stable mechanical properties and oxidation resistance almost up to the solidus temperature of the material. Ni-based superalloys generally contain a large amount of Cr and Co, where Co is added to raise the melting point and Cr is added to increase the corrosion resistance. Some elements such as Cr and Al have very stable oxides even at severe temperatures. These oxides cover the surface as a very thin layer and limit the oxygen, nitrogen, and sulfur diffusion towards the inner parts, providing oxidation and corrosion resistance for the part. It is important to adjust the limits of the alloying elements since the excessive amount can cause TCP formation and increase the risk of segregation which leads to a decrease in strength and operation life [9], [16], [17].

1.2.2 ɣ' (Gamma Prime) Precipitates

ɣ' phase is formed with the constitution of $Ni_3(Al, Ti)$ and it acts as the major strengthening mechanism in most of the Ni-based superalloys due to precipitation hardening. Since this phase also has FCC structure (FCC_$L1_2$), it is coherent with the matrix especially from nucleation to the beginning of the growth. According to the cooling after casting and heat treatment procedures, primary and secondary ɣ' precipitates with varying sizes can be observed in the microstructure. ɣ' particle shape can show variation depending on the interfacial energy between ɣ-matrix and ɣ' precipitates found in the microstructure as spherical, cuboidal, and dendritic morphologies [18], [19], [20], [21].

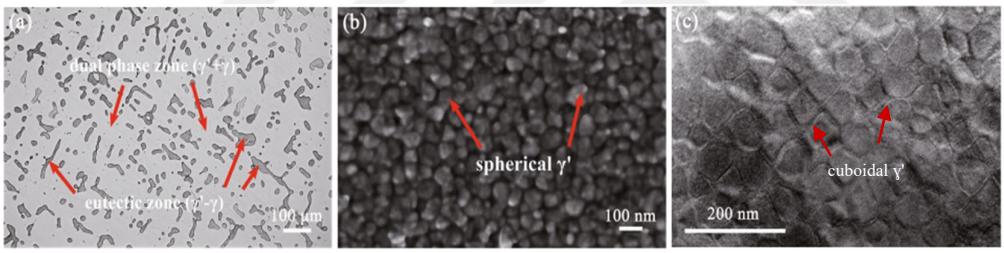

Figure 1-3 (a) OM image of ɣ - ɣ', (b) spherical ɣ' precipitates observed with SEM; (c) cuboidal ɣ' observed with TEM.

ɣ' precipitates increase the material strength at elevated temperatures by limiting the dislocation movements in the matrix. Since ɣ' precipitates are the major strengthening mechanism in most of the Ni-based superalloys, the amount, size, and distribution of ɣ' particles highly affect the material strength. Controlling these three variations in the microstructure, by applying the heat treatment and cooling procedures relatively, results in obtaining strength limits as in the design needs.

In the case of Nb taking place in the alloying of the material, some ɣ' precipiates with Ni_3Al change their formation by replacing Nb with Al and Ni_3Nb phase particles,

which is known as ɣ" precipitates and are seen in the microstructure with $D0_{22}$ (BCT) structure [6], [22].

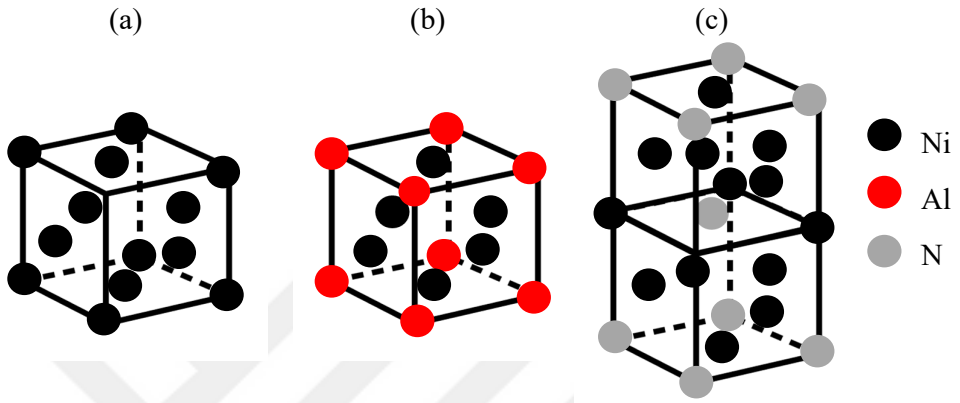

Figure 1-4 (a) ɣ – FCC, (b) ɣ' – FCC_L12 and (c) ɣ" – BCT_$D0_{22}$ structures.

Although the ɣ' particles, especially during nucleation stage, shows coherent interface with ɣ-matrix due to its crystal structure, ɣ" phase particles shows incoherency due to the disruptions of cubic crystal structure which increases the lattice misfit between matrix and precipitates.

1.2.3 Carbides and Borides

A small amount of carbon (from 0.02 to 0.2 weight %) is usually seen in Ni-based superalloys. This addition is usually made on purpose to form the carbides that are beneficial to strength of the material by limiting the dislocation movement, increasing rupture strength, creating nucleation sites during solidification, and controlling the grain size accordingly during heat treatment & long service terms as well as tying up some elements to prevent the unstable phase transformations [23-26]. However, depending on the distribution and morphology of these carbides, they can facilitate the crack propagation, which ends up with the failure of the part. Also,

although these carbides are very stable at room temperature, MC type of carbides highly tend to transform into $M_{23}C_6$ and M_6C type of carbides between 750 – 1000°C, approximately. MC type of carbides is usually seen in spherical shape whereas $M_{23}C_6$ carbides are seen in cuboidal and M_6C carbides in elliptical shape [26-27]. Depending on the composition of the alloy, MC carbides can be found as TiC and WC, which both have spherical shape and coarse particles segregating at matrix or grain boundaries in transgranular or intergranular positions and between dendrites. $M_{23}C_6$ type of carbides can be found as $Cr_{23}C_6$ in the grain boundaries in smaller and more irregular shapes than MC carbides. Controlling the amount of $Cr_{23}C_6$ carbides is important to keep the corrosion resistance of the alloy, where absence of Cr in the solid solution of ɣ-matrix results with reduced oxidation and corrosion resistance of the part. M_6C carbides can be seen in the microstructure if Mo and W alloys have more than 6-8 weight percentage in the material [6].

Borides can be found in the Ni-based superalloys in a much smaller amount compared to the carbides. They also contribute to the rupture strength, creep resistance, and grain size control by forming M_3B_2 and M_5B_3 types. Since boron has low solubility in ɣ-matrix, it is important to limit the B amount in the alloying to prevent the segregation of these borides [6], [26].

1.2.4 Topologically Close Packed (TCP) Phases

TCP phases such as μ ($(Fe, Co)_7(Mo, W)_6$), σ ($(Fe, Mo)_x(Ni, Co)_y$), and Laves ($(Fe, Cr, Mn, Si)_2(Mo, Ti, Nb)$) are commonly found in Ni-based superalloys due to the long exposures to high temperatures. These phases can be formed either in heat treatment applications or during the service. These phases are formed if the alloy microstructure and composition are not stable and BCC transition metals such as Cr, Ta, Nb, Mo, and W have high ratios in the alloy composition.

TCP phases have mostly needle-like and plate-like shapes with extreme hardness promoting cracking and failure in the material by decreasing the ductility and creep

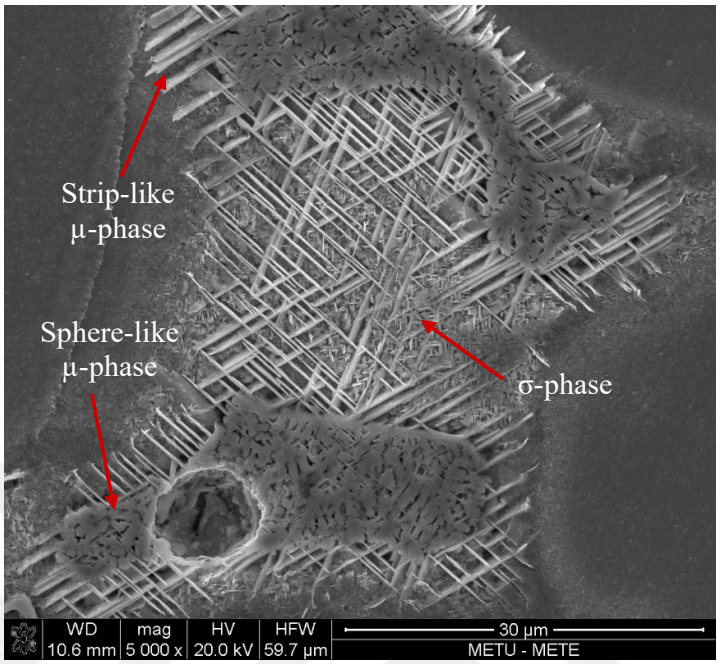

Figure 1-5 TCP phase representation observed in Udimet720 superalloy with SEM at 5000X.

rupture strength of the part. These phases also reduce the amount of some elements as Mo, Cr, and Fe where these elements contribute to the solid solution strengthening of ɣ-matrix and corrosion resistance of the part [6], [27-29].

1.3 Heat Treatment of Ni-based Superalloys and Modelling

Ni-based superalloys are designed for working under extreme conditions. Therefore, the material is expected to show good mechanical properties at elevated temperatures reaching up to 0.7 T_M of the related alloy. In order to maintain those strength values at elevated temperatures, materials are developed with stable phases free of inclusion, segregation, and void while having homogeneous microstructures. To have the regularity in microstructure, a good control on the manufacturing processes is required. Also, dissolving the unwanted phases in the microstructure and homogenizing the material with solutionizing results with uniform material

properties and prepares a good starting point for further steps. On the other hand, matrix strength in these alloys are relatively low for the required operational conditions. Therefore, Ni-based superalloys usually undergo heat-treatment processes to have precipitation hardening and a major increase in the strength of the material. This procedure is also called aging and its aim is to nucleate and growth ɣ' particles up to a designed size and amount in the microstructure.

Conventionally casted products such as Waspaloy may contain small porosities in the interdendritic areas even though triple melting is applied. These type of discontinuites cause degradation in mechanical properties and creep resistance. In order to break the casting microstucture with heterogenous nucleation of grains, dendrites, and porosities, hot forging can be applied to ingots. In hot forging applications, either a open and close die forging, or HIP can be used. These processes basically involve high temperature and pressure to recrystallize the material under load to obtain smaller grains with higher ductility and strength and close the small internal porosities to remove their detrimental effects on the strength. However, these processes require high temperature with long duration, which can cause ɣ' formation and morphology change that reduces the coherency between the matrix and precipitates[30-32]. In order to homogenize the microstructure, solutionizing is applied to those wrought alloys and prepare the microstructure for aging applications.

1.3.1 Solutionizing Treatment

Although Ni-based superalloys undergo highly controlled manufacturing methods, micro segregation and chemical instabilities are always likely to be seen in the microstructure due to the high alloying ratio, varying reactivity levels of elements, and activity of phases. Since the aging heat treatment processes require high temperatures with very controlled conditions for long periods of time (which also have high costs), it is important to start this process with a chemically homogeneous and uniform material. The inhomogeneities that might remain from the production

of the ingot and/or has occurred during the forging can be removed by solution heat treatment. Solutionizing (or solution heat treatment) is applied between the ɣ' solvus and solidus temperature to dissolve ɣ' phase as well as dissolving the elements that cause segregation and diffuse in ɣ-matrix. Although high solutionizing temperatures are required to dissolve the ɣ' particles and obtain a homogeneous ɣ-matrix, insipient melting can occur at the grain boundaries, resulting in the reduction of workability and creep resistance of the part. Therefore, subsolvus solution temperature is chosen if the solutionizing window of the alloy is narrow [33-35].

1.3.2 Aging

Aging heat treatment of Ni-based superalloys carries a big importance and subsequently works on to obtain the required fraction, size and distribution of ɣ' precipitates, leading to the desired mechanical strength values. Generally, Ni-based superalloys undergo two-step aging process where the first step takes place at higher temperatures for shorter periods to facilitate the nucleation and second step is applied at relatively lower temperatures for longer periods to promote the growth of these precipitates [36-37]. This two-step aging technique accelerates the precipitation dynamic and shortens the heat treatment period remarkably, leading to lower energy consumptions. At the end of this aging process, usually bimodal distribution of ɣ' particles is obtained and varying sized particles provide strengthening with both cutting and Orowan looping of dislocations[5], [17], [38-39].

1.3.3 Thermodynamic Modelling with CALPHAD

With the advancements in computer science and increase in its wider availability, some thermodynamic laws that are impossible to solve manually were adapted in high-alloying systems analytically and became solvable for multi-component multi-hase materials. Especially for the materials with high-cost ingredients and long-processing with high temperatures that lead to huge amounts of energy consumption,

providing some solutions to reduce the number of trials for the production of these materials became more important.

Kaufmann, Cohen and Bernstein were the pioneers who adapted the thermodynamic calculation in real alloy systems by providing models for the phase equilibria for binary and ternary systems. CALculation of PHAse Diagrams (CALPHAD) method is developed with numerous computer programs in 1970s and 1980s. Afterwards, developments on these programs focused on multicomponent systems, providing high quality and more reliable thermodynamic decriptions together with the determination of phase temperature profile, solidification behaviour, metastable phases, driving forces of these phases and properties of these phases, which helps to couple with the mechanical properties of a given system [40-42].

The thermodynamic equilibrium of a given system with multiphase equilibria at constant pressure is determined with respect to the summation of molar Gibbs energies of the stable phases, leading to minimum Gibbs energy.

$$G = \sum_{\varphi} n^{\varphi} G_m^{\varphi} \tag{1.1}$$

In the given formula above, n^{φ} stands for the number of moles and G^{φ}_m is for the molar Gibbs energy of phase φ. In software that provide CALPHAD for multi-component systems modeling, frame reference, weighted molar Gibbs energies of the compounds, configurational terms and contributions of other physical phenomena such as magnetism are used for the derivation of the Gibbs energies of phases, and the material under varying temperature and pressure conditions with more complex formulas that helps to model the real-life processes more efficiently [43].

For the Ni-based superalloys, using the Integrated Computational Materials Engineering methods has shown an enormous effect on the alloy design and dramatically reduced the time needed for these designs.

1.3.4 Heat Treatment Modelling

Modeling of heat treatment processes created a big deal in the superalloy industry to predict the amount and size of strengthening phases as well as observe TCP formations in the microstructure that cause a decrease in mechanical properties and degradation in creep rupture strength. Differently from the solidification modeling, mobility of the elements and kinetics of the phases are needed together with the thermodynamic properties of the constitution to perform the precipitation modeling. The precipitation model usually performed in Ni-based superalloys is known as the Langer-Schwartz-Kampmann-Wagner Numerical Model, and is also detailed in this part of the study.

1.3.4.1 Precipitation Nucleation and Growth

As mentioned before, the CALPHAD method is developed to perform thermodynamic calculations and determine the phase diagrams, accordingly. As this method is improved in time, applying kinetic calculations has also become possible by using the related databases formed either experimentally or together with ab-initio calculations. Ni-based superalloys are one of the metal alloy groups for which CALPHAD is frequently used. There are many studies in the literature that employ PANDAT [44-46].

Second-phase precipitated particles and their characteristics have an enormous effect on the properties of engineering alloys such as mechanical strength, toughness, creep, and corrosion resistance, especially in Ni-based superalloys operating under severe conditions. The nucleation, growth, and coarsening behaviors of these particles can vary depending on the high-temperature range and cooling rate.

During the heat treatment of metals, many precipitation models become applicable such as the Langer-Schwartz theory, the Kampmann-Wagner numerical model (KWN), classical nucleation theory, the simplified growth model developed by Morral and Purdy, and the SFFK (Svoboda-Fischer-Fratzl-Kozeschnik) model for complex systems (which is also applicable for the varying shape evolutions of precipitates) [47-50].

Classical nucleation theory explains the nucleation behavior of second-phase particles in the matrix in two different manners, namely homogeneous nucleation and heterogeneous nucleation.

In homogeneous nucleation, precipitates are expected to occur everywhere on the material, and calculations are done by considering the material properties such as chemical driving force, elastic strain energy, and effective diffusivity of the matrix. The nucleation rate for homogeneous nucleation is set as [51-52]:

$$J = N_v Z \beta^* \, exp\left(-\frac{\Delta G^*}{k_B T}\right) exp\left(-\frac{\tau}{t}\right) \tag{1.2}$$

Where N_v is the nucleation site density, Z is the Zeldovich factor, β^* is the atomic attachment rate, t is time, τ is the incubation time for nucleation, k_B is Boltzmann constant and T is temperature.

On the other hand, heterogeneous nucleation is expected to occur on dislocations, grain boundaries, grain edges, and grain corners where the determination of potential nucleation sites and nucleation barrier become more important. Effective interfacial energy also needs to be calculated alongside the interfacial energy between matrix and second phase particle for the determination of heterogeneous nucleation.

Classical nucleation theories also have evolved with the participation of effective diffusivity terms that are clarified in the SFFK model. [53-56]

A simplified growth model was introduced by Morral and Purdy in 1994 to explain the growth and dissolution of precipitates with different morphologies. This model considers the Gibbs-Thomson effect where the solubility limits are modified and equilibrium phase transformation, solidification, and precipitation are completed with respect to the Gibbs free energy of the phases and the system, for the multiphase and multicomponent systems. The growth of spherical particles is defined as [50], [57-58]:

$$v = \frac{dR}{dt} = \frac{K}{R}\Delta G_m^* \tag{1.3}$$

where K is kinetic parameter, and ΔG_m^* is the transformation driving force.

On the other hand, the SFFK (Svoboda-Fischer-Fratzl-Kozeschnik) model explains the precipitate evolution with the radii and chemical composition of individual particles that are taking place in different phases in a multi-phase and multi-component system. A simplified version of the SFFK model can be described as [59]:

$$A(t) = \frac{2\sigma}{R_g T}\left[\sum_{i=1}^{n} \frac{(c_{ki}-c_{oi})^2}{c_{oi}D_{oi}}\right]^{-1} \tag{1.4}$$

where c_{ki} is the molar concentrations of alloying element in the particle and c_{oi} is in the matrix phase, R_g is the gas constant, and T is the absolute temperature. D_{0i} is the diffusivity of the element in the matrix and σ *is* the interfacial energy.

This model was also developed in time by Kozeschnik and Svaboda by taking the shape factor under consideration and re-creating the model in a way that is not only applicable for spherical but also suitable for needle and disc-like particles. The model contains a set of linear equations that can all be solved together to determine the particle growth rate and composition change rate of all the precipitate phases [48-49], [51], [56], [60].

1.3.4.2 Langer-Schwartz-Kampmann-Wagner Numerical Model

Langer and Schwartz have developed a theory explaining the nuclation, growth and coarsening of droplets in the metastable in 1980 with mean-field approach. Langer and Schwartz assumed a phase seperation in a simple two-component fluid to simplify the system. The proposed theory by LS decribes the concurrent nucleation and diffusion controlled growth of the particles as a function of size and time assuming a set shape for size distribution where only the precipitates that have a size larger than the critical radius belong to that distribution. As the different equations obtained after these assumptions are combined, below formula was obtained where $\overline{r_{LS}}$ is the mean radius, N_{LS} is the total number of precipitates, C_B^{β} and $\overline{C_B}$ are the mean composition of component B in the precipitate and matrix, respectively.

$$\frac{4\pi}{3}\overline{r_{LS}}^3 \cdot N_{LS} \cdot \left(C_B^{\beta} - C_B^0\right) = (C_B^0 - \overline{C_B}) \tag{1.5}$$

Wendt and Haasen adapted this theory to the Nickel alloys for the ɣ' precipitation and solid solutions in 1983. The result of the study showed that long exposure times

to elevated temperatures at 650°C increase the ɣ' particle density while keeping the particle radius constant at the initial stages of aging. However, as the aging stage reaches the middle of the design process, ɣ' particles start to grow whereas the particle density drops as also stated in Liftshitz-Wagner theory. To explain this decomposition behavior, a modification of the Langer and Schwartz model is made by Wendt and Haasen [61].

$$\frac{d\bar{R}}{dt} = \frac{\overline{dR}}{dt} + \frac{1}{N_v}\int_{R^*}^{\infty}(R-\bar{R})\dot{j}\,dR + (\bar{R}-R^*)\frac{N_R(R^*)}{Nv}\frac{dR^*}{dt} \qquad (1.6)$$

Where, $\bar{R}$ is the mean particle radius, R^* is the critical radius of particles, Nv is the number of atoms found in a unit volume and $N_R(R^*)$ is the number of particles in particle size distribution with $R^* \pm \Delta R^*$ per unit volume and unit radius.

Kampmann and Wagner have developed a numerical model in regards to non-linear Gibbs-Thomson relation and added it to Langer-Schwartz equation with the implementation of an emprical time-dependent factor on steady state nucleation rate for the observation of transient nucleation kinetics that is seen in the experiments. The LSKW approach provides a macroscopic precipitation modelling starting from nucleation and continuing with growth and coarsening of the precipitates together with the CALPHAD thermodynamic databases and is most commonly used in the complex alloy systems with multi-component and multi-phase transformations. The model enables tracking the precipitate size distribution throughout the heat treatment period as a function of time. The LSKW approach also known as KWN (Kampmann-Wagner Numerical model) is a mean-field model assuming that the nucleation take place homogeneously through the matrix and the precipitates form in spherical shape [54], [62-67].

The nucleation rate (Equation 1.7) and growth rate (Equation 1.8) with the KWN model are constructed with the formula:

$$J(t) = J_s \, exp\left(-\frac{\tau}{t}\right) = Z\beta^* N_0 \, exp\left(-\frac{\Delta G^*}{kT}\right) exp\left(-\frac{\tau}{t}\right) \tag{1.7}$$

$$\frac{dR}{dt} = \frac{C(t)-C_R}{C_P-C_R}\frac{D}{R} \tag{1.8}$$

Where J_s is stationary nucleation rate, τ is incubation time, N_0 is number of potential nucleation sites per unit volume, β^* is the rate of solute atoms in matrix joining the nucleus, C_P is the concentration of the solute in the precipitate, $C(t)$ is the concentration of the solute in the matrix and C_R is the concentration of the solute in the interface boundary.

1.4 Strengthening Mechanisms in Ni-based Superalloys and Modelling of Yield Strength

Ni-based superalloys used in turbine engines operate under severe conditions, namely high temperatures and mechanical loads. These materials are usually strengthened by many different mechanisms and determining the strength of the material with a physical-based model becomes more complex due to the interaction of those mechanisms with each other as a consequence of composition and phase fraction.

Although there are many different mechanisms as detailed below, the directions of those mechanisms affecting the total yield strength change. For instance, the main

strengthening mechanisms' contribution to the ɣ-matrix strength are solid solution strengthening, grain size strengthening, and lattice strength of Ni. On the other hand, ɣ' particles provide precipitation hardening. In addition to those mechanisms, as a result of ɣ' existence in the microstructure and solid solutioning elements, strengthening due to the blockage of dislocation motion either via cutting or looping contibutes to the overall yield strength of the material.

Ni-based superalloys with a polycrystalline microstructure have high yield strength values either dominated by ɣ-matrix with solid solutioned elements or via precipitation hardening with respect to the size and amount of ɣ' particles. Designing the material and selecting the strengthening mechanism can be completed by choosing the material with respect to the operation conditions.

1.4.1 Strengthening Mechanisms in Ni-based Superalloys

Strengthening of Ni-based superalloys is obtained mainly with precipitation hardening with the existence of secondary phase particles as ɣ' and solid solution strengthening. Although the major strengthening is obtained with these two mechanisms, grain size/boundary strengthening and dislocation hardening also contribute to the mechanical properties of these alloys.

The yield strength prediction can be done with respect to the linear summation method as:

$$\sigma_y = \left(\sigma_{ss}^n + \sigma_{ph}^n + \sigma_{Oro}^n + \sigma_{gh}^n + \sigma_{coh}^n + \sigma_0^n\right)^{1/n} \quad (1.9)$$

Where n is between 1 to 2, σ_y is yield strength, σ_{ss} is solid solution strengthening, σ_{ph}^n is precipitation hardening due to particle shearing, σ_{gh} is grain size hardening,

σ_{oro} is dislocation hardening due to Orowan looping, σ_{coh} is coherency strengthening and σ_0 is the lattice strength of pure Ni.

1.4.2 Precipitation Hardening

The phenomena of precipitation hardening was introduced starting from the 1910s and developed by Orowan, Taylor, and Polanyi with the implementation of the role of dislocations [68]. After that, by using TEM imaging, Kelly and Nicholson illustrated the mechanism behind the precipitation hardening, and Brown and Ham showed a better understanding of precipitate–dislocation interactions [68-70].

Precipitation hardening is the major strengthening mechanism in most of the Ni-based superalloys causing a barrier effect by the particles to the dislocation gliding and blocking the dislocation motion either by shearing or looping mechanisms. The second phase particles also show an effect on limiting the grain boundaries due to their positioning on the open structures as the matrix and keep their effect until their dissolution in the matrix above approximately 1030°C where the solutionizing temperature needs to be determined carefully to prevent the grain growth in the microstructure which leads to decrease in mechanical properties [71-77].

In the case of applied stress is smaller for the penetration of dislocations to precipitates, where usually the incoherent precipitates with larger precipitate sizes are seen in microstructure, Orowan bowing is seen in the microstructure where the dislocations with lower stress bow between the particles [78-79].

$$\sigma_{oro} = M\frac{3\mu b}{2\lambda} \tag{1.10}$$

The equation can be solved as where μ is shear stress, *M* is Taylor's factor, λ is mean interparticle spacing, and *b* is burgers vector.

An extended equation for the calculation of Orowan dislocation looping strengthening is also introduced as [68], [70], [80-82]:

$$\Delta\sigma_{orowan} = M\frac{0.4Gb}{\pi\sqrt{1-\upsilon}}\frac{ln\left(2\sqrt{\frac{2}{3}}r/b\right)}{\lambda} \tag{1.11}$$

$$\lambda = 2\sqrt{\frac{2}{3}}r\left(\sqrt{\frac{\pi}{4f}} - 1\right) \tag{1.12}$$

where G is matrix shear modulus, υ is the Poisson's ratio of the matrix, f is volume fraction of precipitates and r is the mean radius of precipitates.

On the other hand, if higher stress is applied to the precipitates having lower particle size with increase in the coherency between ɣ' particles and matrix, enhancing the possibility of penetration of dislocations to the particles and particle shearability - cutting of particles- by the dislocations occur and the need for calculating the coherency strengthening as well as ordered domain strengthening prediction becomes more important since these become the major strengthening mechanism for the material. These particles can be found in the microstructure with varying sizes and chemical compositions. A typical precipitation hardening as a result of shearing is described as [78]:

$$\sigma_{Ph} = M\frac{\gamma_{APB}l_1}{2b(A_1+r)} \tag{1.13}$$

Where γ_{APB} is anti-phase boundary energy between matrix and precipitate, l_1 is the length of dislocation cutting the precipitate and A_1 is the distance between the

precipitates. Depending on the weak and strong pair coupling of matrix and precipitate, the length of the dislocation cutting plane can change and affect the precipitation hardening contribution to the yield strength.

For the cutting of precipitates (shearing), it is important for the ordinary dislocations to continue their motion in pairs in order not to destroy the order supplied by ɣ' with the ordered FCC_$L1_2$ structure. In the case of shearing smaller ɣ' particles, weak coupling occurs since the dislocation pair cannot lie within an individual particle. However, for the precipitates with a size (diameter) greater than 20 nm, strong coupling occurs since the following dislocation enters the same precipitate before the previous dislocation exits as shown in Figure 1-6. Both of these pairing types cause APB formation which affects the strength of the material [79].

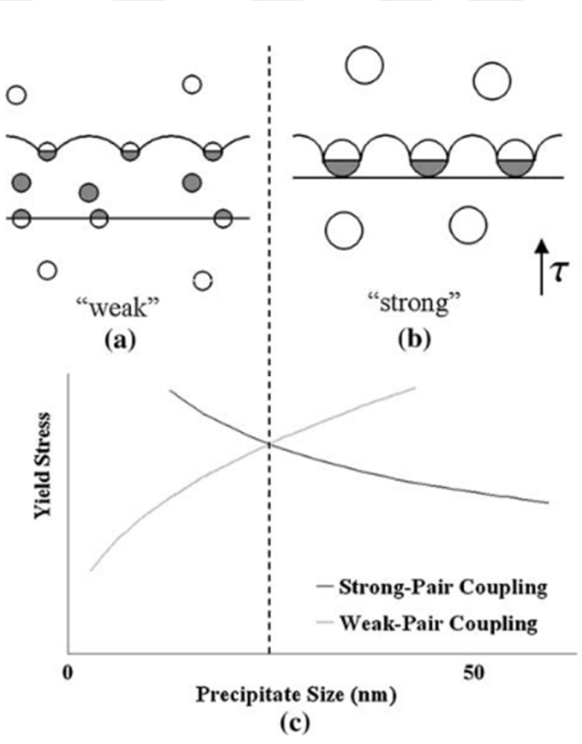

Figure 1-6: Effect of particle size (c) on the yield strength due to weak pair coupling (a) and strong pair coupling (b).

Anti-phase boundaries are planar defects in the material that occur when the atoms are found in the interface with correct atomic positions for the discussed ordered phase structure but have the wrong chemical nature. These anti-phase boundaries form on the slip planes if matrix dislocations shear the ordered and coherent particles like ɣ' particles with FCC_$L1_2$ structure in Ni-based superalloys and create APB on the slip plane of the precipitate. The APB energy has an anisotropic characteristic and the term is explained with respect to the unit area of the slip plane cutting the particle. γ_{APB} can be calculated as [72], [83].

$$\gamma_{APB} = \frac{2.42 k_B T_c S^2}{a^2\sqrt{3}} \tag{1.14}$$

Where S is the long-range order parameter, a is the lattice parameter, k_B is the Boltzmann's constant and T_c is the critical ordering temperature.

After the shearing of precipitates occurs, new phase boundaries are formed with relatively low interface energy that still needs to be overcome by the dislocations for the deformation to continue. This mechanism of additional hardening as a result of shearing is called chemical strengthening where the contribution of chemical hardening is quite low and negligible for aged alloys [68].

Due to the cutting of particles or with the looping of dislocations around the precipitates, Ni-based superalloys are mostly hardened with the precipitation of ɣ' phase. Although those mechanisms rely on the antiphase boundary hardening occurring from the coherency of ɣ', some studies are conducted to investigate the effect of the coherency strains arising from the lattice misfit on the overall yield strength of the material [84]. Strengthening due to lattice misfit arises from the stress

fields around the interface at which the precipitate is coherent with the matrix. Those stress fields restrict the dislocation gliding, and the contribution of this misfit is explained by Brown and also as [68-69], [82]:

$$\sigma_{misfit} = MxG(\varepsilon)^{3/2}\sqrt{2f\frac{r}{b}} \tag{1.15}$$

$$\varepsilon = |\delta|\left[1 + 2G\left(1 - 2v_p\right) / G_P(1 + v_P)\right] \tag{1.16}$$

$$\delta = \frac{a_P - a}{a} \tag{1.17}$$

where χ is material constant changing from 2 to 3, ε is the misfit strain parameter, G_P is shear modulus of precipitates and υ_P is the Poisson's ratio of the precipitates, δ is the difference between lattice parameters of precipitate a_P and matrix a.

Goodfellow et. al. also mentioned the same model for the calculation of coherency strengthening as [78]:

$$\sigma_{coh} = M\alpha G\delta^{3/2}\left[\frac{f\gamma^{\prime}r}{b}\right]^{1/2} \tag{1.18}$$

This equation can be solved where α is material constant, δ is lattice misfit and $f\gamma^{\prime}$ is precipitate volume fraction.

The difference between precipitate atoms' radii and matrix atoms' radii explains the coherency of the interface between matrix and second-phase particles where the dislocation motion whether increase the system energy due to the blockage of dislocation motion occurs or not. An increase in the particle radius increases the incoherency between the precipitate and the matrix, and the dislocation energy becomes insufficient for cutting the particles and favored to Orowan looping [85-86].

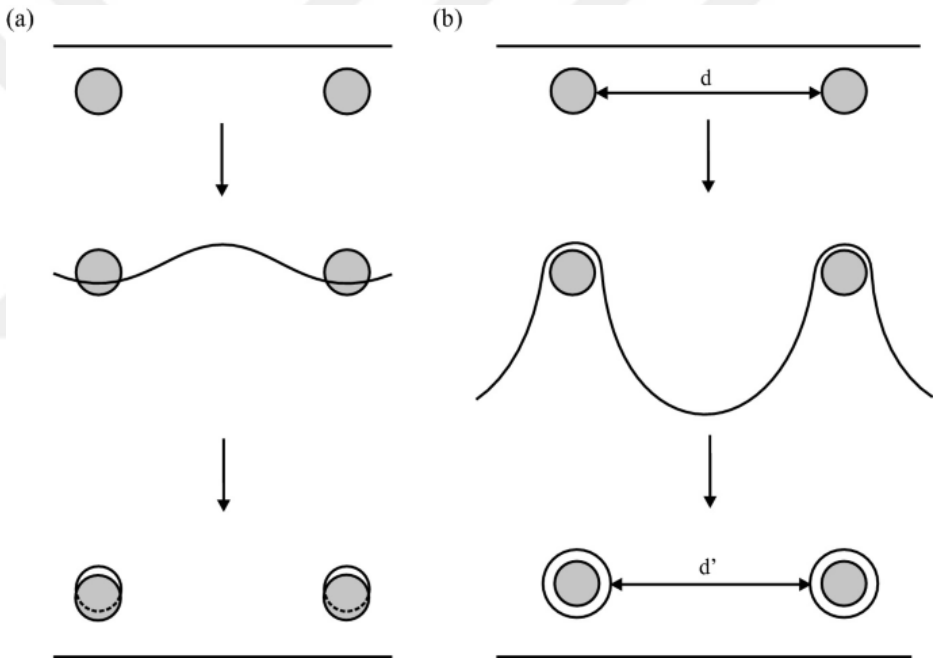

Figure 1-7 A schematic illustration for dislocation cutting (a) and bowing (b) mechanisms.

Especially for materials with uniform precipitate size, one of these mechanisms is favored and the dominant mechanism is chosen with respect to the critical radius that also explains the coherency between the matrix and the second phase particles varied during aging as shown in Figure 1-8 and can be taken as 10*b where b is the burger vector [86-88].

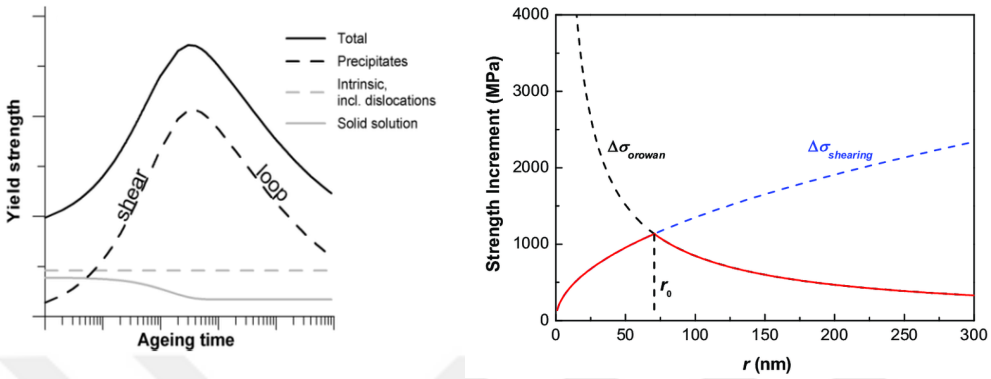

Figure 1-8 Tendency of yield strength increment with precipitate size through aging (left) by dislocation shearing and bypassing (Orowan) mechanisms (right).

Therefore, depending on the radius of the precipitates, the system is dominated by either shearing or Orowan looping which eliminates the contribution of other precipitation hardening to the overall strength of the material. That is why most of the Ni-based superalloys are designed to have bi-modal size distribution to benefit from the contribution of both shearing and looping strength as well as coherency strengthening that arises after the shearing of particles.

1.4.3 Solid Solution Strengthening

Solid Solution Strengthening mechanism helps the material to keep the mechanical strength of the alloy at elevated temperatures due to the elements solved in ɣ-matrix such as Mo, Fe, Cr, and W. Therefore, the volume fraction of phases and the composition is the main criterion for the prediction of this strengthening mechanism.

Strengthening due to solid solution occurs where the solute element with higher strength dissolves in the solvent metal and either replaces the host atom or places between the host atoms, causing localized lattice distortions. These distortions interact with the dislocations and strengthen the material either by dislocation

locking due to size mismatch, modulus mismatch, and stacking-fault interaction or dislocation friction [89]. Since solvent atoms are favored to place near the dislocations where they can interact with the stress fields caused by the dislocations as lattice distortions, these atoms with size mismatch are more likely to interact with edge dislocations [90]. On the other hand, solute atoms in the matrix result in variation of shear modulus both with the interaction of screw and edge dislocations [91]. Stacking fault occurs in a plane if a plane is removed/added, which in turn changes the order of the solvent as ABCABABC or ABCABCCABC, causing planar defect. Some solute atoms are also favored to segregate on the crystal structure, causing a separation of partial dislocation, blocking the dislocation motion, and increasing the strength of the material [5], [92]. Also, the interaction of dislocations and solute atoms during the dislocation gliding causes frictional forces increasing the strength of the material. The amount of strengthening is related with the concentration of solute atoms in the matrix that act as an obstacle to the dislocation motion [89-90], [93].

The solid solution strengthening formula varies for the ordered and disordered phases [94-96]. Since both ɣ-matrix and ɣ' precipitates have ordered structures, below formula introduced by Fleischer can be used for the prediction of strength contribution via solid solution [91]:

$$S_i^{\gamma} = \Sigma \beta_i^{\gamma} \left(x_i^{\gamma}\right)^{\frac{1}{2}} \tag{1.19}$$

Where β_i^{γ} is a constant set for each element and depends on the atomic size and modulus, x_i^{γ} is the atomic percent of element in the ɣ-matrix.

In order to calculate the solid solution strengthening of the elements above to the ɣ-matrix can be predicted using the equation [78]:

$$\sigma_{ss}^{\gamma} = (1 - f_{\gamma'})[\Sigma(S_i^{\gamma})^2]^{1/2} \quad (1.20)$$

By using the same equations above with the addressing parameters, it is also possible to calculate the solid solution strengthening in ɣ' phase particles.

1.4.4 Grain Size/Boundary Strengthening

Grain boundary strengthening is often explained with blocking the dislocation motion by absorbing its energy or dividing the dislocations in pieces due to the misorientation between consecutive grains in polycrystalline materials. Therefore, the grain boundaries are considered as stationary impediment to the dislocation motion, where the increase in grain boundaries results in an increase in the yield strength of the material. In those boundaries, dislocation pileups, partial or total transmission of dislocations stored at the grain boundary or obtained from the parent grain to the adjacent grains including the parent grain with or without leaving partial dislocations in the grain boundary result in grain boundary strengthening as seen in Figure 1-9 [97]. In the case of precipitate or segregation presence at grain boundaries, dislocation pinning can also be seen in addition to the mechanisms mentioned above.

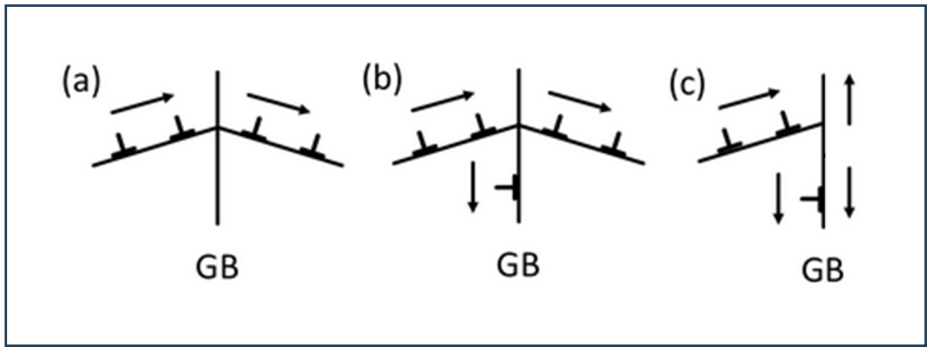

Figure 1-9: Dislocation motion variation at grain boundaries: (a) direct transmission of dislocation, (b) partial transmission by leaving residual dislocation at GB, (c) accumulation of dislocations at GB causing pileups.

The grain size effect on yield strength is described by the Hall-Petch equation [98]:

$$\sigma_y = \sigma_0 + \frac{k_y}{\sqrt{D}} \tag{1.21}$$

Where k_y is the Hall-Petch constant that varies depending on the alloy, D is the grain size and σ_0 is the friction stress that is a summation of all the mechanisms hindering the dislocation motion as precipitation hardening, solid solution hardening, and Orowan and/or coherent strengthening. Thus, the effect of grain size hardening by itself can be calculated as:

$$\sigma_{gh} = \frac{k_y}{\sqrt{D}} \tag{1.22}$$

Since hot forging application facilitates the recrystallization, refining of grain size is obtained in wrought superalloys which increases the contribution to the total yield strength of the part. However, the contribution of grain size hardening to the yield strength is observed as the least effective mechanism among the ones above in aged Ni-based superalloys [78].

1.5 Waspaloy Superalloy

Waspaloy is developed by Pratt & Whitney Aircraft in the 1950s as a Ni-based superalloy to use compressor and rotor discs, shafts, spacers, blades, rings, and casings. This alloy shows superior high-temperature strength due to age-hardening and solid solution strengthening to work under up to 980°C with good corrosion and

notably oxidation resistance up to 650°C. The age-hardening of this alloy is derived from the aluminum and titanium elements with ɣ' particle formation, whereas solid solution strengthening is derived from the contribution of molybdenum, cobalt, and chromium. This alloy is typically manufactured as cast and wrought where casting is applied in three stages, namely VIM, ESR, and VAR.

Aerospace materials such as Waspaloy are designed to work under high mechanical loads at elevated temperatures. Therefore, providing the homogeneity of the microstructure without any irregularities such as inclusions, voids, and segregations causing a reduction in the strength of the part is very critical. In order to eliminate those irregularities, remelting the alloy is crucial.

Vacuum induction melting uses electromagnetic induction and generates Eddy current in the metal conductor to heat the smelting material under vacuum conditions to have better control of the chemical composition of the alloy by preventing contact with hydrogen, oxygen, and nitrogen. Although this method provides a chemical composition almost the same as the final product, melting cannot be completed uniformly; thus, further refining is required.

On the other hand, in Electro-Slag Remelting, an electrical current passes through the slag, and the ingot is protected by the vapor of the slag from the atmosphere. Liquidized material drops into a water-cooled mold with high quality alloying and free of impurities, and the slag pool floats above the refined material. As a result of this flow, the material is obtained as directionally solidified with high purity, low sulfur content, and few non-metallic inclusions.

After this step, the Vacuum Arc Remelting procedure can be applied, by choice, to have more cleanliness, uniformity, fatigue resistance, and fracture toughness of the material. With this manufacturing method, more homogeneous material with a smaller number of inclusions and higher purity can be obtained.

The triple melting method is mostly required in military applications for the control of chemistry and purity of the material where this system is especially important for

the removal of oxide inclusions, metallic inclusions, and micro-segregation which is also known as interdendritic segregation containing the Laves phases [99-100].

As can be seen in Table 1-2 taken from the patent [101], Waspaloy superalloy is designed to have high Cr for oxidation resistance, high Co and Mo for solid solution strengthening, favorable Ti and Al for ɣ' precipitate formation, presence of carbon and boron for carbide and boride phases for the strengthening of material by dislocation pinning mechanisms.

A typical microstructure of Waspaloy consists of ɣ-matrix, ɣ' precipitates, and a minor amount of carbides that occur on the grain boundaries of the matrix [102]. The ɣ' precipitates formed during the cooling of the ingot are called primary ɣ' precipitates, whereas the ones formed during aging are called secondary ɣ' precipitates.

After the casting of Waspaloy, hot forging is applied to the material in order to remove the heterogeneity in the microstructure remaining from VIM – ESR – VAR, closing the micro-porosities and obtaining finer grains. Depending on the need for recrystallization and control of grain growth, the forging of Waspaloy usually takes place between 1000 to 1100°C. [103-104]

Wrought Waspaloy is generally solutionized between 1000 – 1100°C for 4 hours to resolve the transformed carbides that decrease the oxidation resistance of the alloy and some or all of the ɣ' phase particles depending on the need [105-107]. This solutionizing treatment is usually followed by aging where aging of commercial Waspaloy is also completed in two-step at 840°C for 4 hours followed by air cooling and aged at 760°C for 16 hours for nucleation and growth of ɣ' phase particles with bi-modal size distribution with higher material strength [101], [107-109].

Although Waspaloy is developed for a wider range of applications as told before, this superalloy is most commonly used as turbine disc and blade material due to its relatively easier manufacturing processes and yet, tremendous strength with major

strengthening obtained from the ɣ' particles with precipitation hardening and supported by ɣ-matrix with solid solution strengthening [78], [110-111].

Table 1-2: Typical Chemical composition of Waspaloy

Element	Weight Percent
Carbon	0.02-0.10
Manganese	0.1 maximum
Phosphorous	0.015 maximum
Sulfur	0.015 maximum
Silicon	0.15 maximum
Chromium	18-21
Iron	2 maximum
Molybdenum	3.5-5.0
Titanium	2.75-3.25
Aluminum	1.2-1.6
Cobalt	12-15
Boron	0.003-0.01
Copper	0.1 maximum
Zirconium	0.02-0.08
Nickel	Balance

Yield strength of a commercial Waspaloy at room temperature mostly consists of precipitation hardening with about 60% of the total yield strength. The contribution of solid solution strengthening covering both the matrix and the precipitates varies between 12 – 15% depending on the alloying content. The alloy that undergoes shearing of particles by the dislocations is also affected by coherency strengthening with a range of approximately 15% MPa and Orowan strengthening is found to be negligible for this case. Lastly, contribution of grain size/boundary strengthening is

about 5% MPa and pure lattice strength of Ni also needs to be added to the total strength where the overall yield strength for this material is generally changes between 800 to 1000 MPa [17], [78-79].

1.6 Thesis Overview

Ni-based superalloys are very expensive materials due to their numerous components of costly raw materials, hard and long manufacturing methods applied at high temperatures, and their long heat treatment processes as well as testing equipment of produced parts. Therefore, designing a material starting from the raw material to the heat treatment process, and observing the changes in mechanical properties became an important subject, especially in the aviation industry.

This study focuses on the changes in microstructure and their effect on the mechanical properties of the part. Waspaloy is used for creating an independent model for these purposes and the results are compared with the experimental studies.

In Chapter 2, Waspaloy solidification under equilibrium and non-equilibrium conditions is modeled using PANDAT with respect to the CALPHAD method. Experimental studies are conducted on the as-received Waspaloy ingot to investigate the initial microstructure affecting the heat treatment process design.

In Chapter 3, the effect of heat treatment temperatures and durations on the microstructural changes are studied with PANDAT with respect to the Kampmann-Wagner Numerical Model and simplified growth kinetics to obtain a uniform precipitate size distribution with high volume which eases the metallographic analysis. Experimental analysis is conducted by using a curing furnace and TEM for the comparison of precipitate characteristics in the modeling and real-life experiments.

In Chapter 4, the yield strength of Waspaloy is predicted by taking the effects of precipitation hardening, solid solution strengthening, Orowan strengthening, and grain size hardening under consideration at room temperature, 580°C, 650°C, 720°C,

and 1100°C. Analytical results are compared with the experimental results that were completed in the Gleeble 3500 system.

CHAPTER 2

SOLIDIFICATION

2.1 Introduction

In this chapter, the equilibrium and non-equilibrium solidification of Waspaloy is simulated with PANDAT software to compare the obtained results with the as-received material.

Due to their finite solidification rate, commercial casting processes often take place in non-equilibrium or quasi-equilibrium conditions rather than at equilibrium and the Gulliver-Scheil method is used for those non-equilibrium or quasi-equilibrium condition modeling. Solidification rate affects the phase fractions of precipitates [110]. At finite solidification rates, the actual solidification end temperature remains below the solidus temperature, as the solidification of liquid causes the composition to be enriched, usually by alloying elements. Accordingly, since the solid composition gradually increases at each solidification step, composition changes occur in the material at the micro-scale (along the distance between the secondary dendrite arms), which is called micro-segregation [111]. Micro-segregation reduces the homogeneity of the material at the micro-scale, and generally affects the material properties negatively [112]. In the Scheil method, it is assumed that the diffusion in the liquid takes place at an infinite rate and there is no diffusion in solid phases [56]. The equilibrium and non-equilibrium states are considered as the lower and upper end states for solidification, respectively. This approach is widely used for solidification structures' estimation, and accordingly, for the homogenization process' design. Although there are mainly 3 types of the Scheil method, since the manufacturing parameters are confidential and not shared by the manufacturer,

classical Scheil will be used for this thesis study, which assumes the highest solidification and cooling rate not allowing diffusion in solid.

2.2 Experimental Procedure

In this thesis, Waspaloy is used to predict the microstructural evolution during heat treatment and couple the obtained results with the mechanical properties. In order to create the model, chemical analysis with Optic Emission Spectroscopy (OES) is applied to the as-received Waspaloy ingot in 5 different points on the diameter to see the compositional change and check the possibility of segregation in the material. The as-received specimen was produced by VIM – ESR – VAR and delivered as a forged product.

As-received material was cut in 5 different points on the diameter with EDM as can be seen in the illustration below. Samples were embedded in conductive bakelite and ground by 120, 220, 400, 600, 800, 1200, and 2000 μm SiC abrasive papers. All the samples were polished with 9, 6, 3, and 1 μm diamond suspensions. All samples were etched with 2 gr $CuSO_4$ + 40 ml HCl + 40 ml Ethanol (95%) etchant [113]. Specimens were analyzed with SEM and EDS to check the phases and phase constitutions and ImageJ to determine the precipitate size and grain size, and micro-hardness testing is applied with under 1 kgf load to predict the yield strength of the as received material by using the Ashby and Jones and Tabor's relation [114].

$$\sigma_{UTS} = 3 * HV \tag{2.1}$$

PANDAT^{TM} software and PanNi2022_All databases are used in order to simulate the phase formation under equilibrium and non-equilibrium cooling conditions and phases that transform during the solidification are compared with the experimental results.

2.3 Results and Discussion

In order to define the solutionizing and aging temperature for Waspaloy, solidification under equilibrium and non-equilibrium conditions is analyzed. As the as-received specimen's chemical composition is compared with the patent, it is observed that the amounts of all the alloying elements were within the limits.

Table 2-1: Chemical composition of the as-received Waspaloy (without P and S).

Element	Al	B	C	Cr	Co	Fe	Mo	Si	Ti	Ni
Mean wt%	1.44	0.01	0.06	18.9	13.1	0.29	4.34	0.02	2.85	Bal.

With the obtained chemical composition from OES as given in Table 2-1, equilibrium cooling (lever) solidification is conducted between 500 to 1750°C as given in Figure 2-1 and it is observed that the Waspaloy for the given composition is expected to fully solidify with a low amount of TiC and ɣ-matrix at 1312°C where the obtained results are similar with the literature, and the cause of this difference arises from chemical composition and software database, mainly [115].

Table 2-2 Critical phase transformation temperatures in Waspaloy.

Phase	Temperature (°C)
Liquidus	1373
Solidus	1312
ΔT	61
ɣ' Solvus	1036
TiC Solvus	1312
$Cr_{23}C_6$ Solvus	985
Cr_7C_3 Solvus	1029
Mo_3B_2 Solvus	912
μ-phase Solvus	634

Some carbide transformations such as $Cr_{23}C_6$, Cr_7C_3, and Mo_3B_2 boride formation were also expected to form during the solidification where the solvus temperatures for each phase are given in Table 2-2. Trace amounts of Mo_3B_2 that formed after the material is fully solidified are expected to positively affect the creep/tension rupture strength due to controlling grain coarsening during heat treatment, and slowing down the grain boundary sliding mechanism. During the equilibrium cooling, primary ɣ' precipitates are likely to occur with 29 volume percent in the microstructure starting from 1035°C. Below 650°C, μ-phase is also expected to form in the microstructure.

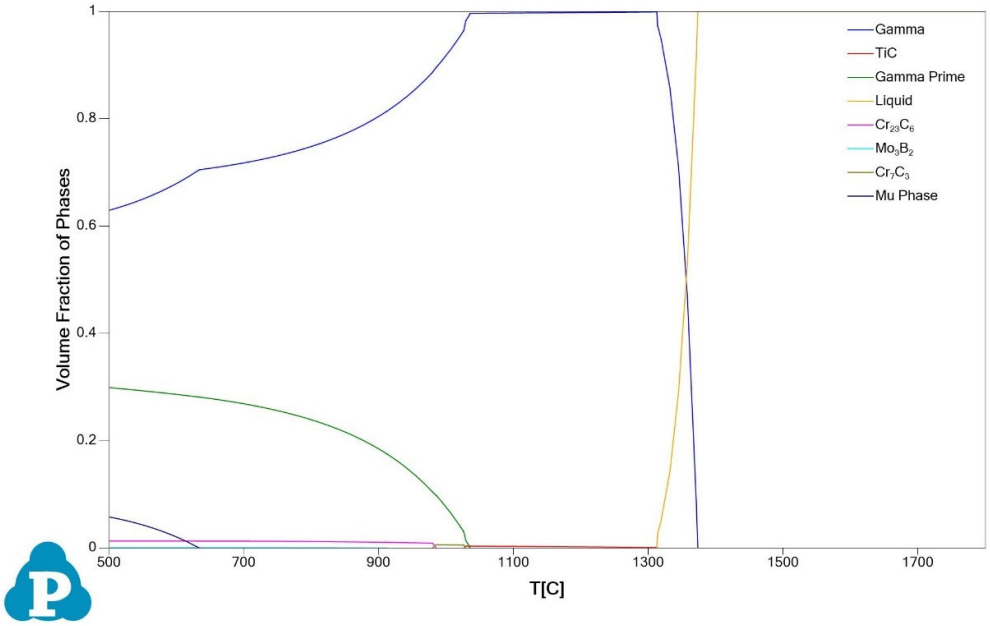

Figure 2-1 Phase transformations in Waspaloy between 500 – 1750°C with equilibrium cooling conditions.

Differently from the equilibrium cooling conditions, non-equilibrium solidification is expected to complete at 1142°C which is about 170°C lower than the equilibrium cooling as given in Figure 2-2. The reason for this variation is related to the enrichment of the liquid with alloying elements due to micro segregation and the corresponding decrease in the melting temperature. Many phases (τ, η, σ) that cannot be seen in the equilibrium state are formed during solidification in the non-

equilibrium state due to segregation. The Scheil-Gulliver approach by assuming the infinitely high cooling rate for the given specimen under non-equilibrium conditions has shown that the ɣ-matrix is the former phase, which is expected form, and followed by the TiC carbides. ɣ' particles are seen beginning at 1180°C and the phase transformations are followed by Eta phase which is a metastable intermetallic that is lost as the solidification is completed. TiB_2 borides are also expected to form as closing to the end of solidification. Lastly, σ-phase, which is a TCP formation, is expected to form and continue its presence in the solidified material. However, it is known that TCP phases can occur in the microstructure after long exposures to elevated temperatures and since the Scheil solidification is a very fast cooling process, it is unlikely that the σ-phase forms and stays in the solidified material.

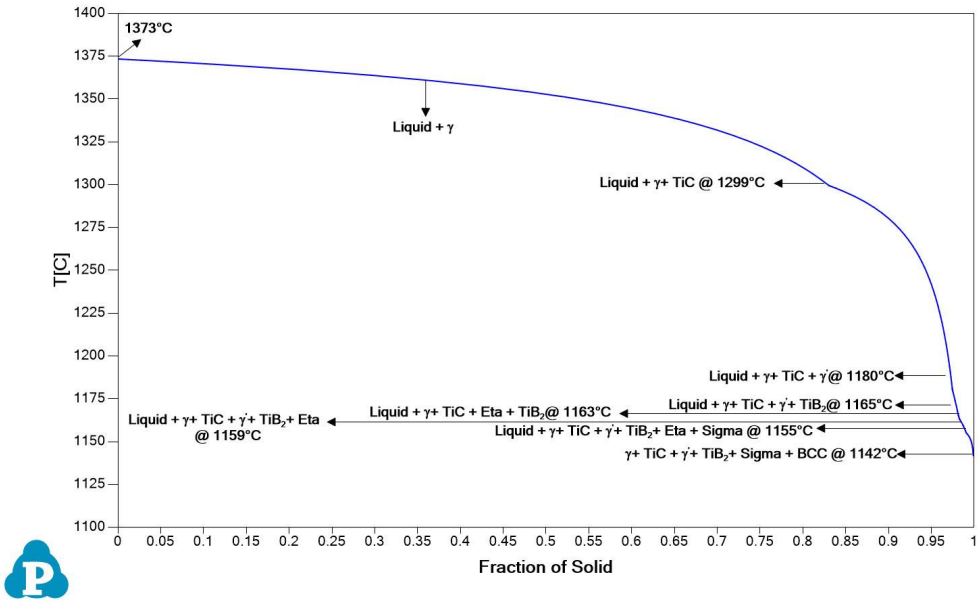

Figure 2-2 Phase transformations in Waspaloy between 1400 - 1100°C with non-equilibrium cooling conditions.

SEM analysis, which is completed on 5 specimens and on 5 different locations in each specimen, has shown that the material had undergone heat treatment most probably during forging application or heat treatment is applied to the ingot since ɣ'

precipitates are seen in the microstructure. EDS has detected the chemical composition of the material quite differently compared to the OES results. Although this is expected for elements with small atomic numbers such as carbon, the very high carbon detection in EDS also affected the amounts of other elements.

Phase constitutions in ɣ-matrix were also analyzed with PANDAT and the results obtained from equilibrium and non-equilibrium solidification are compared with the EDS analysis result of the matrixTable 1-1. Equilibrium cooling results have shown similarity with OES outcomes in most of the elements. The difference in the Al and Ti content can be explained with the ɣ' phase formation where B, C, Mo, and Ti are also related to the possible formation of borides and carbides in the microstructure.

On the other hand, SEM and EDS analysis has shown that the as-received material contains TiC and MoC carbides through the material on grain boundaries varying between 0.05 to 1.5 µm with almost spherical morphology as seen in Table 2-3c and e. ɣ' precipitates were seen in two different morphologies as cuboidal and spherical. Spherical phase particles' diameter varies between 20 to 90 nm, whereas cuboidal ɣ' precipitates are seen in the microstructure between 30 to 200 nm as shown in Table 2-3e.

Table 2-3: (a) Matrix SEM image with SE detector taken under 5000X magnification with ɣ-matrix and ɣ' precipitates, (b) Field EDS analysis of a, (c) Matrix SEM image under 5000X magnification with ɣ-matrix, ɣ' precipitates and some particles, (d) Point EDS analysis showing that the particles are TiC, (e) Matrix SEM image under 40000X magnification with ɣ' precipitates and some particles, (f) Area EDS analysis showing that the particle is TiC.

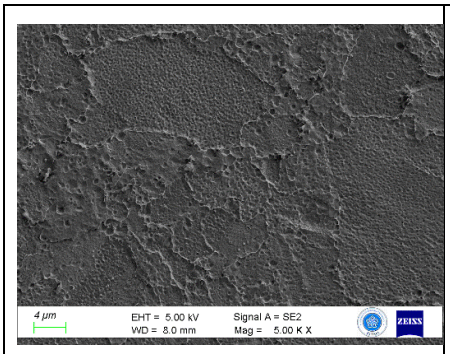

(a)

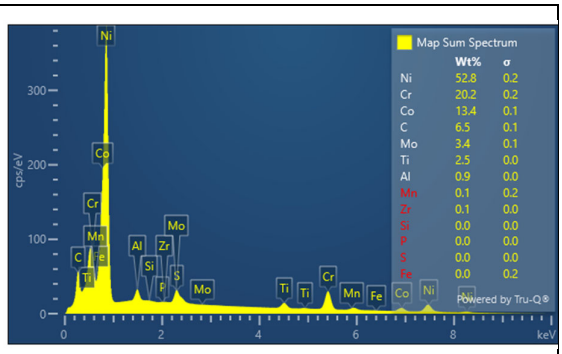

(b)

Table 2-3 Cont'd.

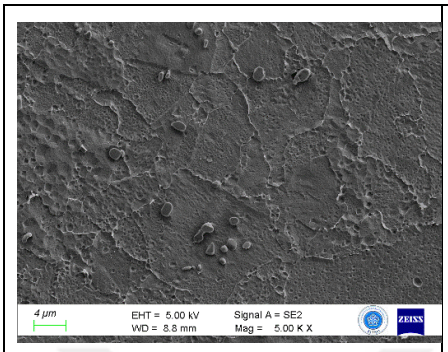

(c)

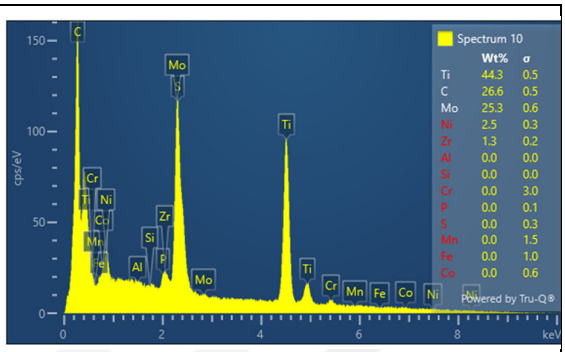

(d)

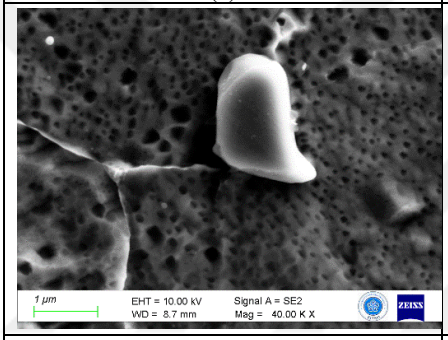

(e)

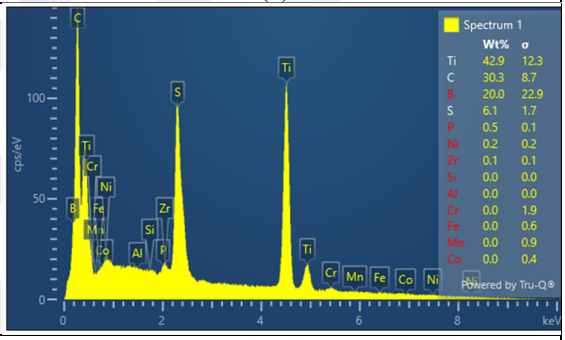

(f)

Hardness measurements from those five specimens with 5 points in each have a result of 454.6 ± 6.5 HV, which corresponds to about 1360 MPa tensile strength at room temperature. This measurement has also shown that the as-received part has undergone an aging process after wrought condition compared to the commercial-aged Waspaloy specimens seen in the literature [101-102], [104-105].

2.4 Conclusion

In this chapter, the effect of the cooling mechanism on the microstructure was modeled to predict the manufacturing and processing method of the as-received Waspaloy ingot. To compare the simulation outcomes with the ingot, several SEM and EDS analyses were conducted, and the results are also supported by micro-

hardness testing outcomes. The conclusions obtained from those comparisons are as follows:

- Results of equilibrium and non-equilibrium cooling solidification have shown that the material with the given chemical composition highly leads to the ɣ' precipitates, carbides, and borides together with austenitic FCC ɣ-matrix. Experimental analysis supported the obtained results in terms of ɣ-matrix and TiC carbide formation. No boride phase is observed in the SEM analysis. It is expected that the boride phase particles have small sizes which makes them hardly observed in SEM.
- Although the as-received material is defined as wrought alloy in the material certificate, a large number of ɣ' precipitates have been detected in the SEM analysis where the amount is much higher than the simulation results. This variation has brought the idea of aged material and to validate the theory, hardness testing was applied, and the results were converted to yield strength. Results have shown that the material has undergone aging processes.

CHAPTER 3

HEAT TREATMENT

In this chapter, experimental and simulation analysis were conducted to optimize the Waspaloy microstructure. As seen in the previous chapter, the received material has shown homogeneous microstructure and remedies of aging. Since the heat treatment modelling requires aging temperatures, cooling rates and exposure times which are not provided by the company, a decision is made as removing the effects of aging by applying solutionizing at 1080°C which is above the ɣ' solvus temperature as seen in equilibrium diagram. After that, in order to obtain homogenous mono-modal ɣ' precipitates with large sizes, an aging process is designed at 850°C for 18 hours as a result of several simulation studies. Simulation and experimental results as well as model details and the experiment setup are detailed below.

3.1 Experimental Procedure

In this study, the as-received Waspaloy ingot with the dimensions of 170 mm height x 155 mm diameter was cut into 130 mm height x 12 mm diameter rods with EDM for heat treatment. EDM cutting parameters were set up as a cutting speed of 0.26 mm/min and a cutting voltage of 47.6 V, and brass wire with 0.25 mm diameter was used for the cutting. A schematic representation of specimen placement on the ingot and EDM cutting pool is shown below.

All heat-treatment applications were done in THERMNEVO – Nevola Curing Furnace where heating is supplied with 6 resistors on each side. Solutionizing heat treatment is applied at 1080°C for 1 hour to the rods with 12 mm diameter followed

by water quenching and aging for 18 hours at 850°C. After aging, water quenching was again applied in order to fix the microstructure for further examination.

Table 3-1 Cutting pool of EDM (a), ingot placement for EDM (b), specimen placement on ingot (c), specimen placement in furnace (d).

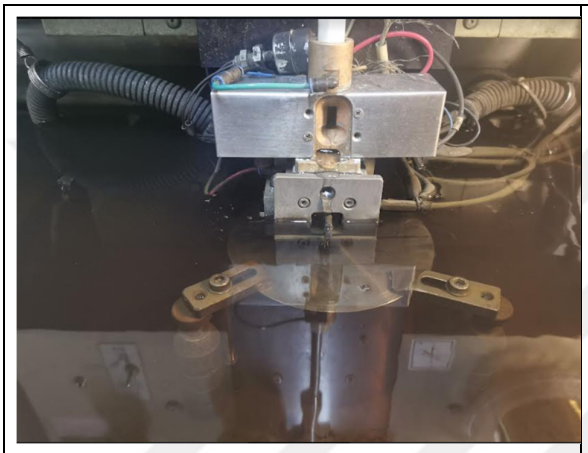	
(a)	(b)
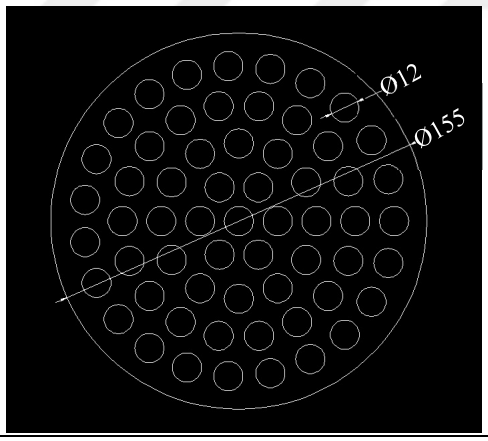	
(c)	(d)

In order to examine the ɣ' precipitate nucleation and growth behavior, 4 samples that were quenched at different stages of heat treatment were prepared for TEM analysis. The list of samples with the heat treatment details can be found below [116]. To determine the preferred orientation of ɣ' precipitates in samples, X-Ray Diffraction method was used by scanning between 20 to 90° with Cu radiation source, and results

were analyzed with Match! Software. 2 thin slices with 0.35 mm thickness were extracted from each sample in axial and transverse directions. Slices were then cut with disc punch and 3 mm diameter discs were obtained. After that, discs were grinded up to reaching 150 µm thickness with a grinding apparatus. A hole was created in the center of each sample with a twin-jet electrolytic polishing device in 10 vol.% perchloric acid solution at 20.5 V, -5˚C conditions. The prepared samples were examined with a JEOL JEM 2100 (LaB6 filament) HRTEM device at 200 kV.

Table 3-2: Heat treatment details of 4 specimens undergone TEM analysis.

Specimen #	Heat-Treatment Detail
1	1080°C – 1 hour + WQ
2	1080°C – 1 hour + WQ + 850°C – 15 min + WQ
3	1080°C – 1 hour + WQ + 850°C – 1 hour + WQ
4	1080°C – 1 hour + WQ + 850°C – 18 hours + WQ

For the simulation of microstructural evolution during the heat treatment process, the PanEvolution module of PANDAT software was used with the PanNi2022_All thermodynamic database. A specific kinetic database file was established for Waspaloy with the data obtained from property determination simulations and literature. ɣ' size, amount, number distribution, and size distribution were determined with respect to the KWN model for nucleation assuming spherical particle formation, and the SFFK model for the growth behavior.

3.2 Results and Discussion

This section investigates the response of Waspaloy to heat treatment processes such as solutionizing and aging, as well as presents the comparison of experimental and simulation analysis.

Solutionizing heat treatment modeled at 1080°C has shown that material contains only ɣ-matrix with 99.67 volume fraction and TiC particles with 0.33 volume fraction.

The elements contributing the ɣ-matrix is also found at that temperature as:

Table 3-3 Amount of element in ɣ at 1080°C.

Element	**Weight %**
Al	1.438
B	7.8E-03
C	0.025
Co	13.15
Cr	18.87
Fe	0.293
Mo	4.336
Si	0.021
Ti	2.74
Ni	Bal.

TEM images taken from sample 1 which corresponds to the condition modeled above have shown that total solutionizing of ɣ' particles occurred and some particles with about µm remained in the microstructure as shown in Figure 3-1. As can be seen in the left image, dislocation pileups occur on the grain boundary and partial dislocations are found in the ɣ-matrix.

Table 3-4 Composition of phases in sample 1 analyzed with TEM – EDS.

Element	Al	Cr	Co	Mo	Ti	Ni
Matrix Composition	1.51	20.98	13.45	4.88	2.83	Bal.
Particle Composition	6.98	17.92	10.59	3.85	13.07	Bal.

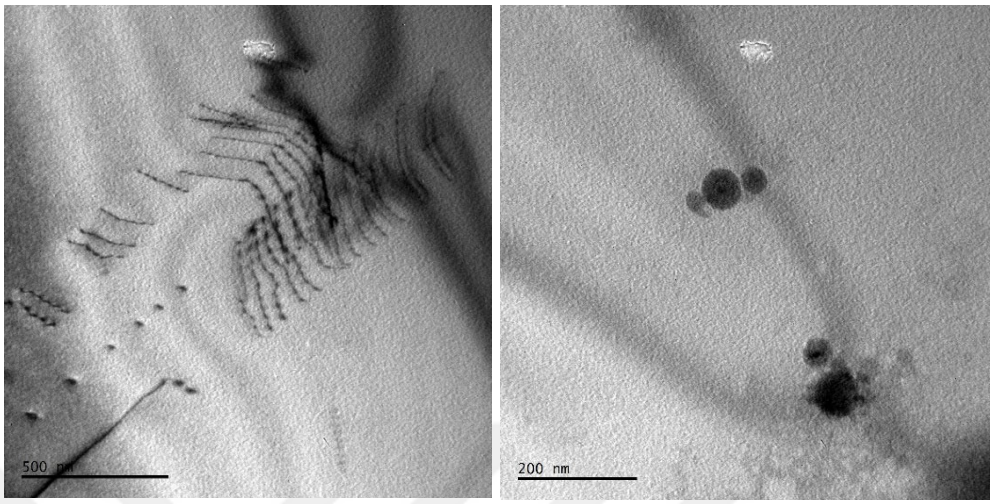

Figure 3-1 TEM image of sample 1: dislocation pile up (left), second phase particle (right).

Although the matrix composition was found similar in TEM – EDS with the simulation outcomes, second-phase particles could not be determined exactly. The composition of the particles given in Table 3-4 brings the idea of ɣ' particles with high Al, Ti, and Ni content where the size of these particles is about 50 nm diameter.

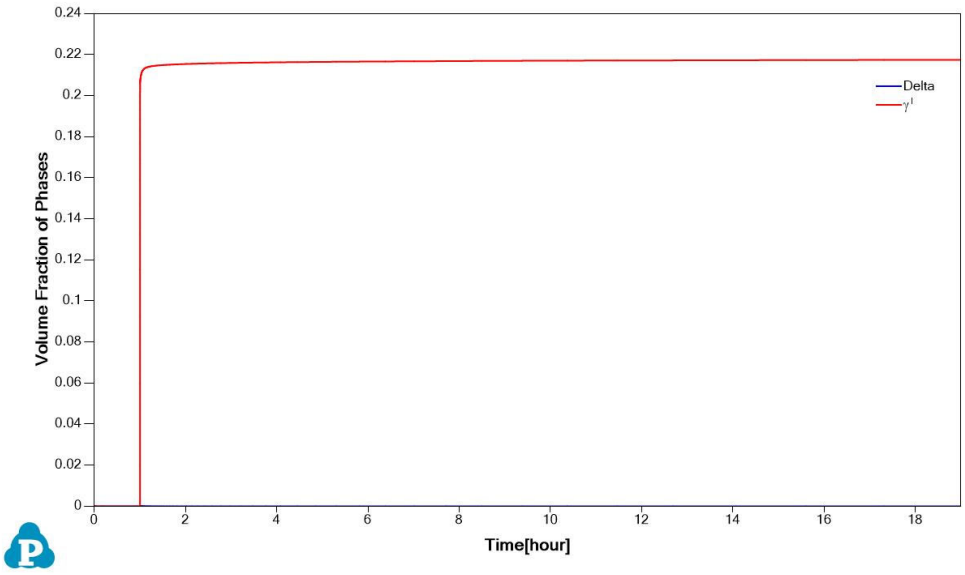

Figure 3-2 Change of ɣ' volume fraction throughout the aging of Waspaloy.

Table 3-5 TEM images, size and volume fractions of ɣ' particles for Sample 2 – 4.

Sample #	Mean Size [nm]	Area Percentage	TEM Image
2	8.5	14.8	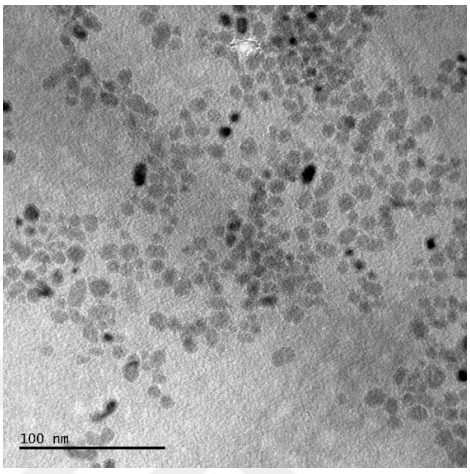
3	17.8	42.6	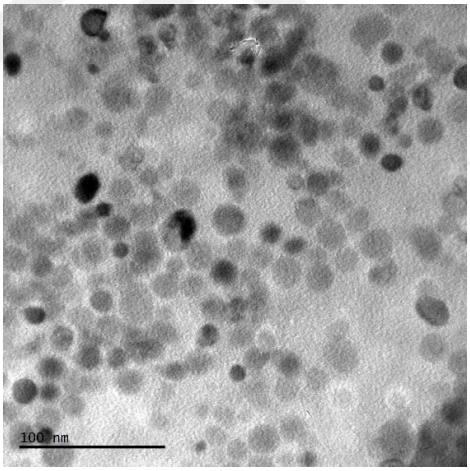
4	50.4	80.9	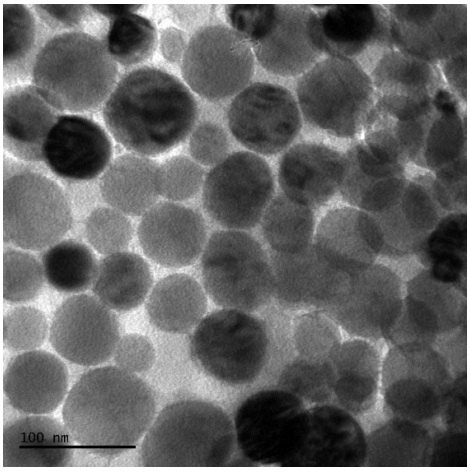

On the other hand, TEM images taken from Samples 2, 3, and 4 have shown numerous spherical ɣ' particles with uniform particle sizes in each sample. The related TEM images, particle size, and volume fractions obtained as a result of the designed heat treatment are given below:

As the modeling that is done with respect to KWN nucleation and SFFK growth has shown a volume fraction of 22 % of ɣ' particles are expected in the material, TEM analysis has shown that the ɣ' precipitates are found in the microstructure with about 80.9 area percent.

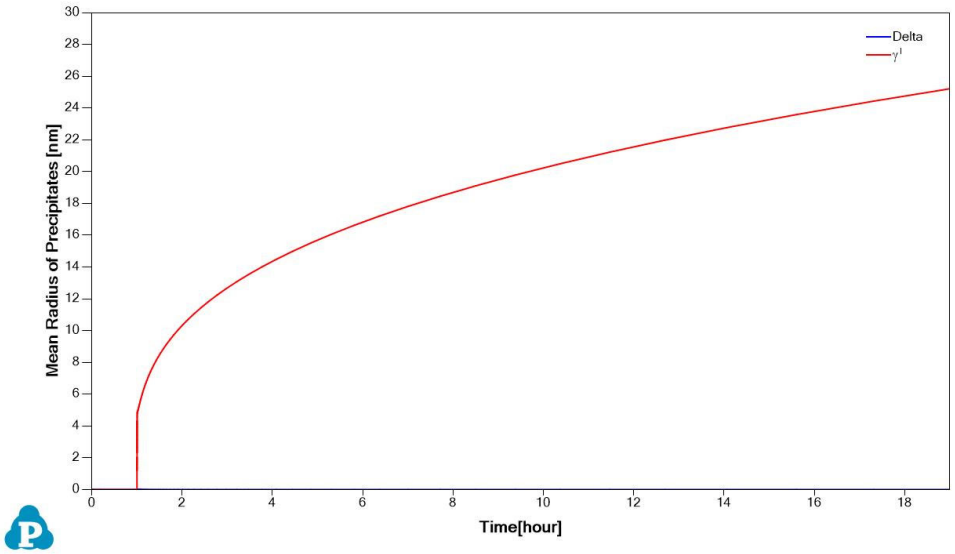

Figure 3-3 Change of ɣ' particle size throughout the aging of Waspaloy.

Although the fraction of ɣ' precipitates did not reflect the real heat treatment process as understood from the TEM images, the size of the ɣ' particles were predicted almost the same as the aging process continues. Simulation results have predicted to obtain precipitates with 0.4 nm radius in the first 15 minutes of aging whereas the TEM analysis has shown particles with about 4.25nm radius in the microstructure. For sample 2, simulation analysis has given a radius of 5.2 nm ɣ' particles at which TEM images have shown ɣ' particles with an 8.9 nm radius. Lastly, both the simulation and TEM analysis gave similar results for ɣ' precipitate radius of 24.8 nm and 25.2

nm, respectively. However, although the simulation setup is prepared for homogeneous nucleation and growth, from the TEM images the nucleation characteristic is seen as semi-homogeneous in the microstructure.

Although the model expected a wider LSW distribution for the radius of the particles with varying sizes, TEM analysis has shown a narrower size distribution mainly focusing on 18 to 30 nm ɣ' particles.

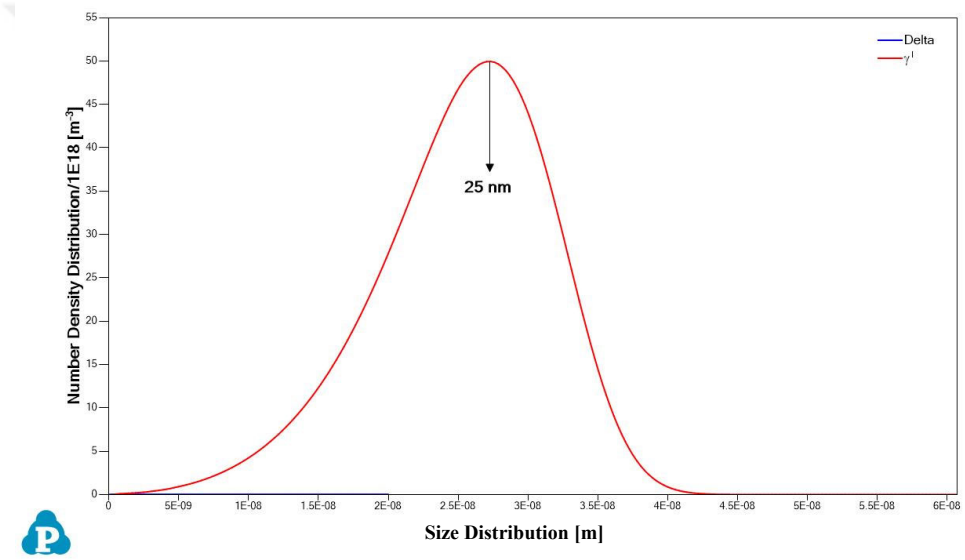

Figure 3-4 Distribution of ɣ' particles with varying sizes.

Even though the modeling studies were completed by taking the Delta phase through the aging under consideration, no formation of the Delta phase has been seen in the analysis results.

From the TEM images of Sample 1, the distance between the dislocations is measured as approximately 97 nm, whereas the distance between precipitates in the images of Sample 4 is analyzed as approximately 21 nm while the calculations according to Equation 1.12 forecasts 36 nm using the modelling results.

3.3 Conclusion

In this chapter, the effect of heat treatment on the microstructure was modeled to predict material strength in the next chapters. To compare the simulation outcomes with the experimental studies, TEM analyses were conducted. The obtained results in this chapter are as follows:

- The modeling results and TEM analysis both showed spherical ɣ' formation with about 25nm size, approximately; however, the fraction of the second-phase particles observed was much higher in TEM analysis than the modeled microstructure.
- A development in the model is required for future studies where the KWN numerical model and the SFFK model with the given kinetic parameters fail to simulate the secondary phase fraction.
- The distance between the dislocations is approximately measured as 97 nm while the distance between the particles at the end of the whole aging process is analyzed as 21 nm.

CHAPTER 4

MECHANICAL PROPERTIES

In this chapter, finalizing the study with the prediction of yield strength by using the outputs obtained in previous chapters is aimed. In order to scrutinize the success of the modeling studies, the material properties are also tested with the Gleeble 3500 system both at room temperature and operational temperatures, as well as around solutionizing temperature. The obtained results are summarized as a function of temperature and outcomes are aimed to compare with the experimental results.

4.1 Experimental Procedure

In this study, the determination of yield strength at different temperatures by using the outcomes of microstructural analysis completed with precipitation modelling is aimed. The specimens that were cut and undergone aging before having undergone machining to the related geometry for the tensile test. In order to simulate the operational conditions, modeling of yield strength is completed for the temperatures of room temperature (20°C), 570°C, 650°C, 720°C with 10^{-3} and 1 strain rate, and 1100°C with 10^{-3} , 10^{-2} , 10^{-1} and 1 strain rate where below and above operational temperatures are examined for a more accurate strength modelling and strength at 1100°C is analyzed for the determination of matrix strength. Experimental studies were conducted at the same temperatures by using the Gleeble 3500 system with SMR311 specimen geometry and HZT71 contact type extensometer with 10 mm gauge length and 2 μm resolution under vacuum up to 10^{-3} Torr where the Gleeble system provides accurate strain rate control by using the data simultaneously collected from the extensometer. Two K-type thermocouples are welded on the specimen for temperature control throughout the experiment with ±5°C and half-contact copper grips are used. Data acquisition rate is set as 1000 data per experiment

to observe changes in the strength with higher accuracy. Free cooling is applied to the specimens after the test is completed.

Figure 4-1: Tensile test set-up.

Experiment results are obtained as true stress-strain graphs where the stress is calculated with respect to the applied force and initial gauge diameter and strain is calculated by using the movement of extensometer arms according to the formulas given below:

$$\sigma = \frac{F}{\left[\frac{\frac{\pi(d_0)^2}{4}L_0}{L_0+\Delta L}\right]} \tag{4.1}$$

$$\varepsilon = ln\left(\frac{L_0+\Delta L}{L_0}\right) \quad (4.2)$$

Yield strength estimation was completed by using the results of equilibrium and precipitation modelling as well as using data obtained from literature.

4.2 Results and Discussion

With respect to the equations described before, yield strength estimation at different temperatures is completed by using the outcomes obtained in Chapters 2 and 3.

From the different equations described in Chapter 1, below equations are chosen for the determination of yield strength of this alloy considering the appropriateness of the data obtained from simulations and found in literature.

Table 4-1 Applied equations for yield strength estimation of Waspaloy.

Strengthening Mechanism	Relative Equation
Orowan Strengthening	$\Delta\sigma_{orowan} = M\frac{0.4Gb}{\pi\sqrt{1-v}}\frac{ln\left(2\sqrt{\frac{2}{3}}r\,/\,b\right)}{\lambda}$ $\lambda = 2\sqrt{\frac{2}{3}}r\left(\sqrt{\frac{\pi}{4f}}-1\right)$
Coherency (Lattice Misfit) Strengthening	$\sigma_{coh} = M\alpha G\delta^{3/2}\left[\frac{f\gamma^{\prime}r}{b}\right]^{1/2}$
Solid Solution Strengthening	$S_i^{\gamma} = \Sigma\beta_i^{\gamma}\left(x_i^{\gamma}\right)^{\frac{1}{2}}$ $\sigma_{ss}^{\gamma} = (1-f_{\gamma'})[\Sigma(S_i^{\gamma})^2]^{1/2}$
Grain Size Hardening	$\sigma_{gh} = \frac{k_y}{\sqrt{D}}$

For the estimation of total yield strength, the linear summation method given in Chapter 1 – Equation 1.9 was used by taking the *n* factor as 1 to eliminate the double confounding possibility of the strengthening mechanisms.

Lattice strength of pure Nickel is also linearly added to the mechanisms given in Table 4-1. All the parameters used in the above equations are given in Table 4-2.

Table 4-2 Model parameters for strengthening mechanisms.

Used Parameters	**Numeric Value**
Lattice strength of pure Ni: σ_0	69 MPa @ RT [117] As a function of T at Appendix C.
Poisson's Ratio: v	0.26 @ RT [117] As a function of T at Appendix D.
Taylor's Factor: M	3 [78]
Shear Modulus: G	80 GPa @ RT [117] As a function of T at Appendix E.
Burger's vector	2.04 Å at RT (a/2<110>) [118]
Interparticle spacing: λ	36.31 nm @ RT (Eqn. 1.12)
Material Constant: α	3.7 [78]
Lattice Paremeter of ɣ	3.59 @ RT [119-120] As a function of T at Appendix F.
Lattice Paremeter of ɣ'	3.57 @ [121-122] As a function of T at Appendix F.
ɣ' radius	25 nm (Ch. 3)
ɣ' volume fraction	22 volume % (Ch. 3)
k_y (T)	250.36 - 0.0738T
Grain size: D	35 µm (Ch. 2)

As the critical radius is stated as 10*b by Kelly et al. [85], the critical radius for this procedure is obtained as 2.5 nm whereas the ɣ' particles after 18 hours aging at 850°C are expected to have 25 nm mean radius. As mentioned before in Chapter 1, dislocations moving along the matrix favors Orowan looping if the particle radius is greater than critical radius.

Although the ɣ' particles are expected to show coherent and homogeneous nucleation on the ɣ-matrix, growth of these precipitates changes the interface characteristic to semi-coherent to incoherent [87]. Therefore, coherency strengthening is also calculated and found as much effective as precipitation hardening mechanism to the yield strength of Waspaloy with the applied heat treatment.

As given in Table 4-3, precipitation hardening due to Orowan looping decreases with temperature mainly due to the change in shear modulus.

Table 4-3 Orowan strengthening in Waspaloy at different temperatures.

Temperature	ν	**b [nm]**	**G [GPa]**	σ_{oro} **[MPa]**
RT	0.31	0.254	80	239.5
580 °C	0.325	0.256	70	200.6
650 °C	0.33	0.256	67	193
720 °C	0.335	0.257	64	185.4
1100 °C	0.34	0.258	50	-

Coherency strengthening is found to be an effective mechanism for this alloy with the given heat treatment procedure. It has been calculated and found that the particles with less than 2.5 nm radius shows coherency with the matrix which corresponds to the nucleation stage. After that, during growth, particles are found to be less than 20 nm where semi-coherent particles are found in the material. This limitation corresponds to ɣ' fraction with 0.04 to use in coherency strengthening calculations.

With precipitates larger than 20 nm where coarsening is observed, the precipitates become incoherent with matrix where these precipitates are no longer a part of coherency strengthening. Coherency strengthening at varying temperatures are given in Table 4-4.

Table 4-4 Coherency strengthening contribution to Waspaloy yield strength at different temperatures.

Temperature	b [nm]	G [GPa]	σ_{coh} [MPa]
RT	0.254	80	235.5
580 °C	0.256	70	204
650 °C	0.256	67	194.9
720 °C	0.257	64	186
1100 °C	0.258	50	-

Solid solution strengthening calculations are completed by using the solidification model results under equilibrium cooling. As stated in Table 4-5, solid solution strengthening obtained from the addition of Cr, Co, Mo, Fe and Al to the Ni results in around 190 MPa strength contribution to the overall strength.

Table 4-5 Solid solution hardening coefficients for the elements contributing in ɣ and atomic fractions of the elements in ɣ [78] and atomic fractions of elements in ɣ at different temperatures.

Coefficient	Al	Cr	Co	Mo	Fe	σ_{ss} [MPa]
β_i^{γ} (MPa/at$^{1/2}$)	225	337	39.4	1015	153	-
x_i^{γ} (RT)	0.0134	0.2846	0.1886	0.025	0.0044	190
x_i^{γ} (@1100°C)	0.0303	0.2064	0.1269	0.0257	0.0029	177

The least effective mechanism among the others is found to be grain size hardening. In the literature, it is observed that grain size of Waspaloy changes from 30 to 90µm[123-125]. Variation of the grain size affects the hardening due to the increasing/decreasing length of grain boundaries interacting with dislocations. However, as given in Figure 4-2, the grain size range of Waspaloy indicated above shows a very little difference in strength as between 24 to 42 MPa where the as-received ingot with average grain size of 35 µm is expected to have 38.6 MPa strength from grain size hardening.

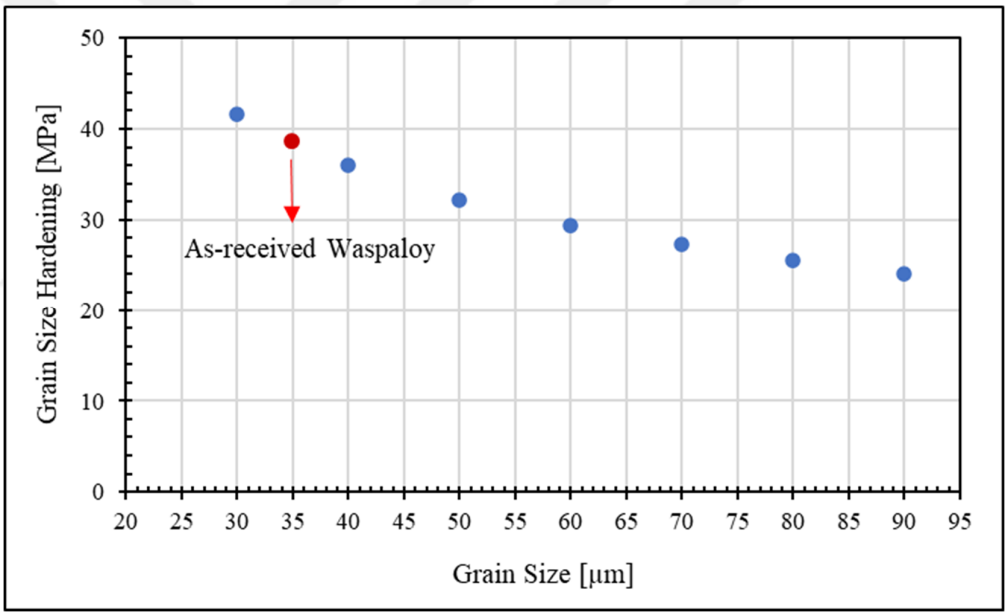

Figure 4-2 Grain size hardening for varying grain sizes.

The effect of grain size hardening for 35 µm grains in average at elevated temperatures are calculated with Hall-Petch constant determined as a function of temperature as given in Table 4-2 has shown that the grain boundary/size strengthening decreases with temperature due to thermal softening as in Table 4-6.

Table 4-6 Grain size strengthening contribution in Waspaloy at varying temperatures.

Temperature	k (T)	σ_{gh}
RT	228.4	38.6
580 °C	187.4	31.7
650 °C	182.2	30.8
720 °C	177.1	29.9
1100 °C	149	25.2

Lastly, the lattice strength of nickel is calculated as a function of temperature as given below. As can be seen in both the figure below and table, the lattice strength of nickel decreases as the temperature increases. This occurs mainly due to the Shockley partials.

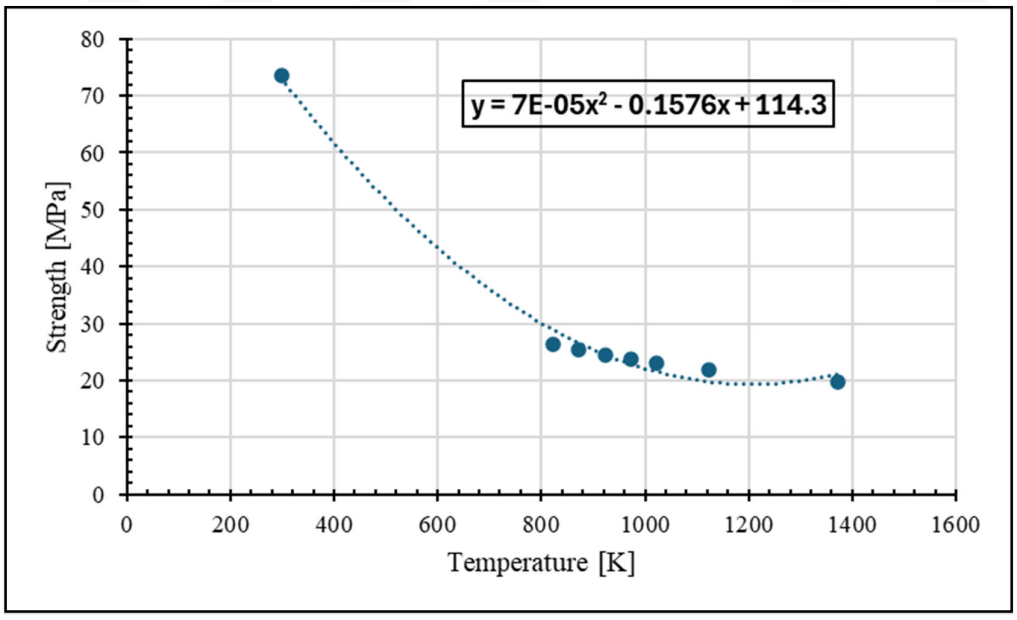

Figure 4-3 Lattice strength of Nickel as a function of temperature.

Shockley partials are found in relatively lower temperatures and causes stacking faults which prohibits the lattice dislocation movements and increases strength. The system is more favored with Shockley partial dislocations' glide due to lower strain energy requirement than lattice dislocations. However, as temperature increases, these partial dislocations unite again and require more energy to move compared with lattice dislocations. Therefore, at elevated temperatures, lattice dislocations become the dominant dislocations due to lower energy requirements.

Temperature	σ_{Ni}
RT	73.6
580 °C	25.8
650 °C	24.5
720 °C	23.5
1100 °C	19.9

By considering the fraction of these precipitates in the microstructure, it can be said that the material act as a composite where the strength of matrix arises from the solid solution strengthening, grain size hardening and lattice strength of base material whereas the second phase provides strength due to the formation of dislocation looping. Lastly, the strength of the alloy also increases from the interaction between matrix and precipitates as in coherency strengthening. The contributions of all strengthening mechanisms calculated analytically by using the outputs of modelling studies has given in Figure 4-4.

On the other hand, the mechanisms active at 1100°C are expected as lattice strength, solid solution strengthening and grain size hardening due to the absence of ɣ' particles. For this reason, major strengthening mechanism at this temperature is found to be solid solution hardening and the expected yield strength with the lead of alloying elements in the matrix has shown a decrease to 188 MPa range.

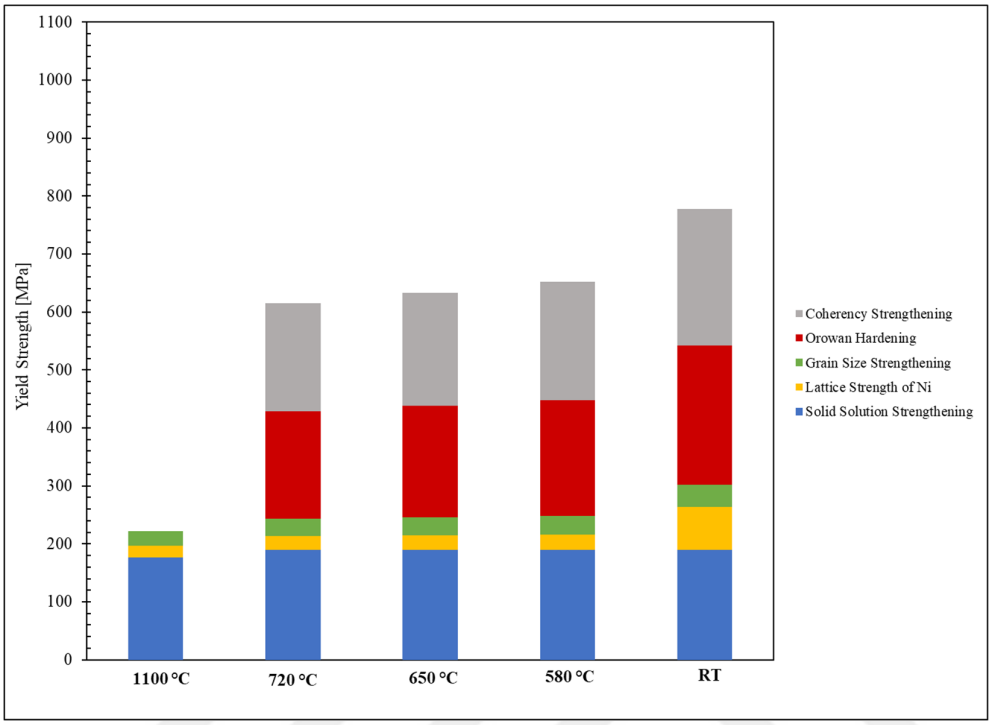

Figure 4-4 Yield strength estimation of Waspaloy at different temperatures.

To validate the modelling studies, experimental analysis was conducted under different strain rates. As given in Figure 4-5 and Figure 4-6, at room temperature, 580°C, 650°C and 720°C, specimens were generally deformed till 0.2 strain in both strain rates whereas the matrix is deformed up to 0.26 true strain under 0.001 strain rate and 0.7 strain under 1 stain rate. The continues lines in the figures show the average of all repetitions whereas the dash lines are presenting remaining repetitions after the others ended up in rupture in previous stages.

For the experiments applied with 0.001 strain, it has been seen that the room temperature properties of the material are superior to with respect to the ones at elevated temperatures both in yield and ultimate tensile strength. After that, the property of this alloy shows better deformation kinetics and strength at 650°C than 580°C and 720°C which explains the design criteria of this alloy where it operates

in the turbines generally around 650°C. On the other hand, Waspaloy has given about 90 MPa of ultimate tensile strength which is way lower than the expected value.

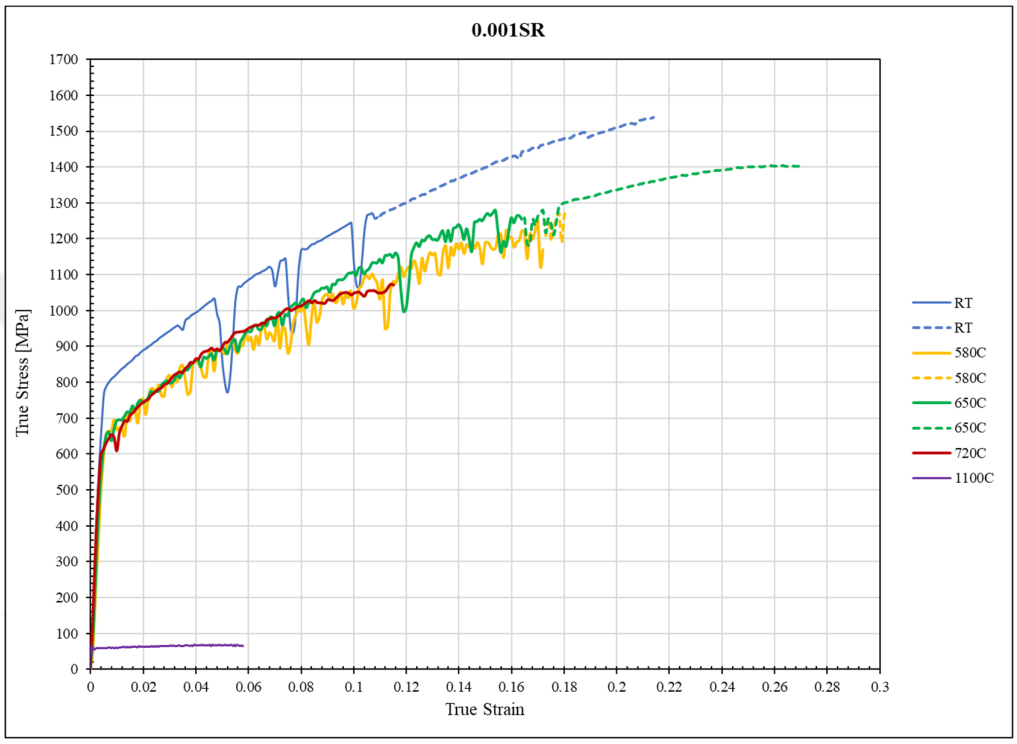

Figure 4-5 True stress - true strain graph of Waspaloy under 0.001 strain rate at RT, 580°C, 650°C, 720°C and 1100°C.

As the results for different temperatures are also compared for 1 strain rate, all the conditions have given an increase in material strength compared to 0.001 strain rate. The trend was similar in both cases as highest strength at room temperature followed by operation temperature with a deformation up to 0.2 true strain. Although the UTS values increased around 100 to 300 MPa with the higher strain rate, yield strength at the same temperature in both conditions showed similar characteristics which explains the strain rate sensitivity for this material only in plastic regime as also seen in other Ni-based superalloys [126-127]. Additionally, 1 strain rate deformation at

1100°C has given rise to about 200 MPa yield strength which is more convenient compared with the modelling results as well as elongating till 0.7 true strain.

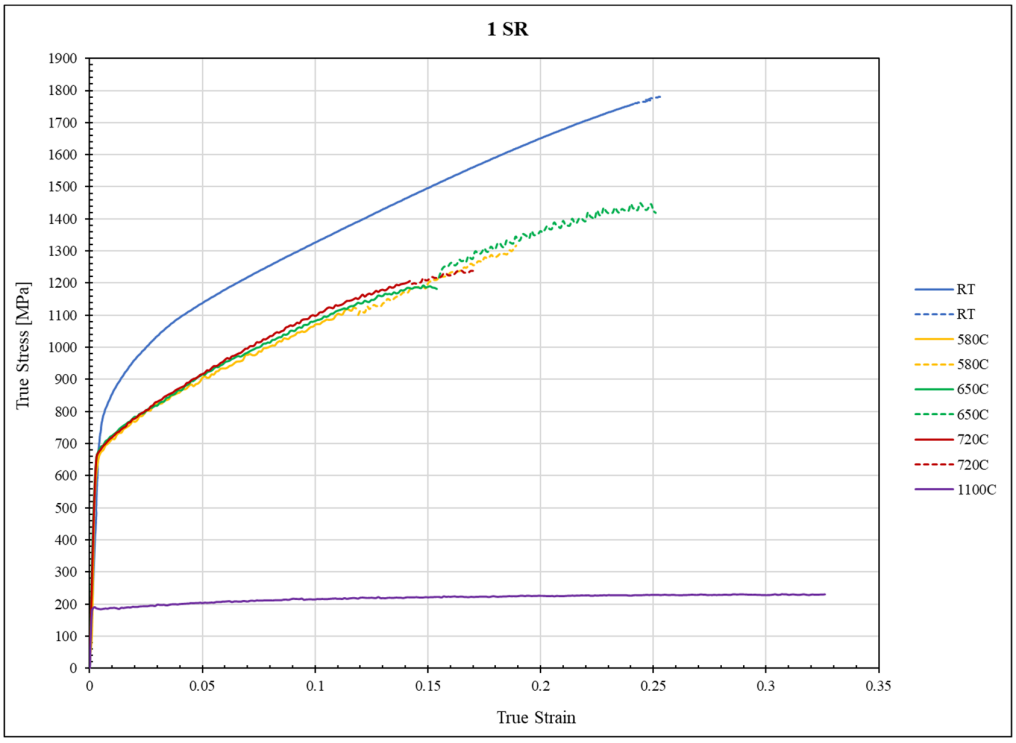

Figure 4-6 True stress - true strain graph of Waspaloy under 1 strain rate at RT, 580°C, 650°C, 720°C and 1100°C.

As observed from the repetitions of the same testing condition, the variations mostly occurred in the beginning of experiments. These variations can be arising from the heat treatment application that completed in two different part affecting the microstructure as ɣ' particles with different fraction and size, machining of the specimens due to abrasion of cutting tool which affects the surface quality of the specimens or the other inhomogeneities in the as-received material such as carbides remained from the casting of the ingot. Standard deviations for these experiments are given in Appendix I.

The modelling and experimental results are given Figure 4-7 and Table 4-7 for a better comparison. It is observed that the modelling studies differ from the experimental results between 7 to 130 MPa, approximately.

The calculations have shown that the experimental and model results give quite good agreement from room temperature to elevated temperatures. Although there are small differences, the variation for the temperatures in this range are assumed to be arising from the microstructure which stabilized after aging and only some carbide and boride formation is allowed as seen before at Figure 2-1. Therefore, the variation mainly arises from the matrix composition and solid solution hardening, relatively since the solid solution constants are used at all temperatures with the room temperature values.

However as seen below table and figure, yield strength at 1100°C is highly overestimated. This estimation was again conducted by using the solid solution constants at room temperature. Summing only the lattice strength and grain size hardening at this temperature gives around 45 MPa where the experimental results has shown around 53 MPa leaving a gap to be filled by solid solution strengthening due to alloying elements in ɣ matrix. However, the difference is much larger than 8 MPa where this variation also supports the idea of using inappropriate solid solution constants for the given temperature.

Table 4-7 Modelling and experimental yield strength results at varying temperatures.

Temperature	**Model [Mpa]**	**Experiment [Mpa]**
RT	792.4	777.8 ± 49.4
580 °C	673.9	656.6 ± 4.8
650 °C	665.7	658.9 ± 13.5
720 °C	674.1	619.3 ± 29.7
1100 °C	187.9	53.1 ± 4.7

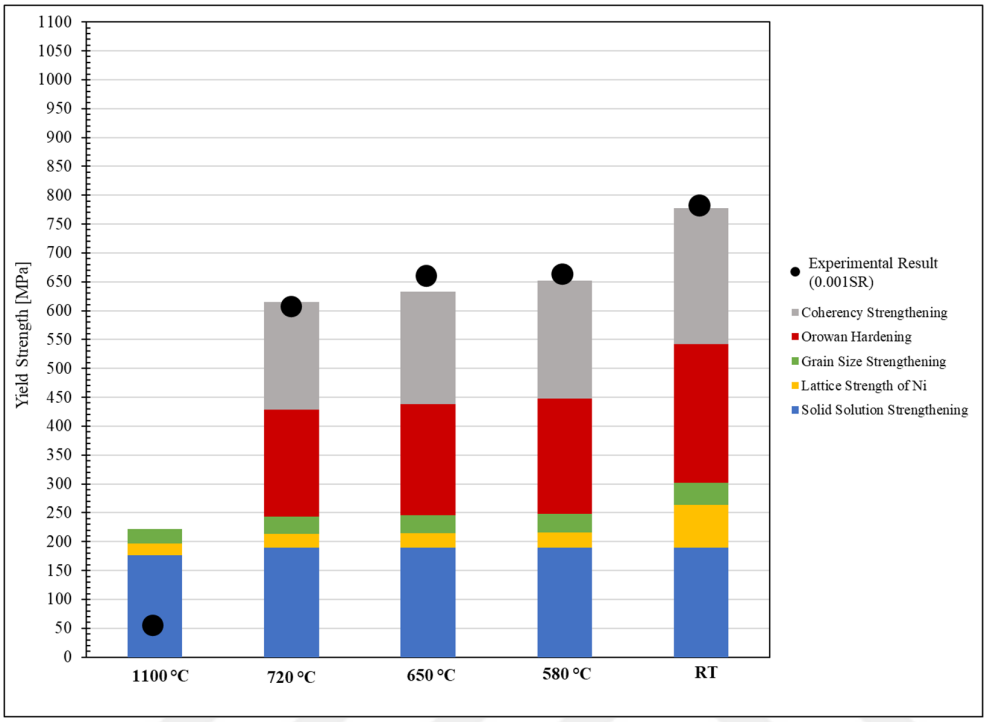

Figure 4-7 Yield strength results from modelling studies and experiments.

Although the model and analytical solutions show a better fit with the experimental ones at RT, 580°C, 650°C and 720°C; yield strength at 1100°C is overpredicted about three and a half times of the real values.

4.3 Conclusion

In this final part of the thesis work, the material strength was calculated by using the parameters obtained in previous chapters and the modelling results were compared with experimental results conducted at both room and elevated temperatures. It is observed from the modelling studies that the strength of Waspaloy mainly arises from the precipitation hardening due to Orowan looping for the applied heat treatment procedure. Therefore, size and amount of ɣ' particles has a great

importance on the material strength where solid solution strengthening, coherency strengthening, and grain size hardening mechanisms are also observed in the alloy.

The thermo-mechanical characterization tests have also shown that the alloy has about 660 MPa yield strength at operating temperature whereas higher strength values are obtained at room temperature and lower ones are got in 1100°C due to dissolution of ɣ' particles in the ɣ-matrix.

The modelling results have shown good agreement with the experimental results in most of the conditions. However, there are possible reasons for the difference between the results:

1. Carbides and borides did not been taken under consideration in the modelling studies and only ɣ-matrix and ɣ' particles are modelled.
2. Only mean precipitate size is used for the analytical solutions and the precipitates with sizes under critical radius that undergoes shearing are ignored due to missing modelling for volume fractions of small precipitates.
3. The aging modelling studies are constructed from the property model outcomes, literature data and some default parameters generated for other Ni-based superalloys which does not 100% represents the inputs for Waspaloy.

Although this study did not reflect the reality for some conditions such as 1100°C, the modelling studies showed a great success from 1 to 8 % error for the room and elevated temperatures where the operational conditions are modelled.

CHAPTER 5

SUMMARY

Waspaloy superalloy is mostly used as turbine disc and blade material in aerospace and power plant applications. The performance of superalloys is expected to endure high temperatures and mechanical strengths exerted upon the material through such applications. Materials working under such conditions mostly undergo different heat treatment procedures to set the microstructure at a point which does not evolve further during operational conditions. The choice of heat treatment parameters changes from one material to another depending on the initial microstructure, required microstructure, and needed thermo-mechanical properties during service. Therefore, determination of heat treatment parameters has a great importance for this materials.

In this thesis work, mechanical properties of Waspaloy for the applied heat treatment procedure has been estimated with modelling studies and analytical calculations. In order to validate the model, physical experiments are also conducted.

Firstly, as received Waspaloy ingot was analyzed for the determination of chemical composition and initial microstructure. The obtained results were compared with the model outputs also by using the literature data. Although the model sets the phases with ɣ-matrix and TiC carbides; the SEM images has shown that the microstructure contained ɣ' precipitates pointing out that the as received ingot has gone under heat treatment. With the solidification modelling outputs by analyzing both equilibrium and Scheil solidification, a solutionizing temperature was set at 1080°C to dissolve the ɣ' precipitates.

As the specimens were analyzed with TEM, it has been observed that the microstructure was only containing ɣ-matrix and some carbides after solutionizing. The modelling studies has concluded that 18 hours at 850°C provides ɣ' precipitates

with 25 nm radius and 22 volume % in the microstructure. For the validation of aging model, heat treatment is applied to the specimens with 12 mm diameter and 130 mm height at 850°C for 18 hours. TEM images taken after aging has shown that the ɣ' precipitates were having an average of 25.2 nm radius with around 81 area percent in the microstructure. Although the size of the precipitate has shown a good correlation with the model, fraction of the precipitates varied largely. The difference is explained with two main points: the variation between area and volume percentage and the images taken from the specimen at where ɣ' precipitates are found more such as close to grain boundaries.

After completing the aging modelling, the yield strength of the Waspaloy for the given heat treatment procedure is calculated analytically at room temperature, around operational conditions (580°C – 650°C – 720°C) and at 1100°C where only ɣ-matrix is expected to be found in the structure. Due to the presence of ɣ' precipitates, precipitation hardening contribution to yield strength due to Orowan looping has been estimated. Following that, coherency strengthening is determined for the precipitates expected to show coherent and semi-coherent characteristic with the matrix with less than 20 nm precipitates size. It has been found that the coherency strengthening and Orowan strengthening are the two main strengthening mechanisms for Waspaloy with the given aging parameters. These are followed by solid solution hardening as a result of alloying elements in the matrix, grain size hardening and lattice strength of Nickel.

The linear summation method is applied to estimate the yield strength by using all the results obtained from strengthening mechanisms mentioned above at room temperature and elevated temperatures by using the model outputs obtained in heat treatment model. For the validation of yield strength estimation, thermos-mechanical tensile tests are conducted at the same temperatures with 0.001 strain rate to minimize the effect of strain hardening. The physical and modelling studies has given a good agreement from room temperature to 720°C with between 1 to 8 % error; however, the yield strength at 1100°C is overestimated. It is explained as the difference between modelling and experimental results can be arising from

the solid solution strengthening where the solid solution constants are found in literature for room temperature strengthening calculations.

The modelling studies performed through this thesis work have given a good correlation with the experimental results precipitation modelling at all temperatures. Additionally, the model set for yield strength estimation is capable of reflecting the thermos-mechanical properties from room temperature to 720 °C which is above the operational temperature of Waspaloy. However, the model needs further improvement for the yield strength estimation at 1100°C by investigating the solid solution strengthening contribution mainly conducting a parameter analysis for solid solution constants.

REFERENCES

[1] R. Noroozian and P. Asgharian, “Microturbine Generation Power Systems”, *Distributed Generation Systems: Design, Operation and Grid Integration*, Elsevier, pp. 149–219, 2017.

[2] Y. Demirel and V. Gerbaud, “Using the Second Law”, *Nonequilibrium Thermodynamics*, Elsevier, pp. 187–265, 2019.

[3] D. Quattrochi, “3.7 Brayton Cycle”, Available: https://web.mit.edu/16.unified/www/SPRING/propulsion/notes/node27.html

[4] M. T. Boyraz, “IN 738 LC Microstructure Optimization with Heat Treatment and Simulation to Improve Mechanical Properties of Turbine Blades”, Middle East Technical University, 2018.

[5] Roger C. Reed, *The Superalloys : Fundamentals and Applications*, Cambridge University Press, 2006.

[6] J. R. Davis, *ASM Specialty Handbook: Heat-Resistant Materials*, vol. 1. ASM International, 1997.

[7] E. Balıkçı, “Microstructure Evolution in Polycrystalline IN738LC in the Range 1120 to 1250”, February 1999.

[8] “Turbine Shaft Forging | Somers Forge.” Available: https://www.somersforge.com/sectors/turbine-shaft/

[9] B. Geddes, H. Leon, and X. Huang, *Superalloys: Alloying and Performance*, ASM International, 2010.

[10] D. Mukherji, J. Rösler, P. Strunz, R. Gilles, G. Schumacher, and S. Piegert, “Beyond Ni-based superalloys: Development of core-based alloys for gas turbine applications at very high temperatures*”, International Journal of Materials Research*, vol. 102, no. 9, pp. 1125–1132, 2011.

[11] W. Xia, X. Zhao, L. Yue, and Z. Zhang, “A review of composition evolution in Ni-based single crystal superalloys”, *Journal of Materials Science and Technology*, vol. 44. Chinese Society of Metals, pp. 76–95, May 01, 2020.

[12] H. Long, S. Mao, Y. Liu, Z. Zhang, and X. Han, “Microstructural and compositional design of Ni-based single crystalline superalloys — A review”, *Journal of Alloys and Compounds*, vol. 743. Elsevier Ltd, pp. 203–220, Apr. 30, 2018.

[13] A. Sato, A.-C. Yeh, T. Kobayashi, T. Yokokawa, H. Harada, T. Murakumo, J. X. Zhang, “Fifth generation Ni based single crystal superalloy with superior elevated temperature properties”, *Energy Materials*, vol. 2, no. 1, pp. 19–25, Mar. 2007.

[14] T. Ning, T. Sugui, Y. Huajin, S. Delong, Z. Shunke, and Z. Guoqi, “Deformation mechanisms and analysis of a single crystal nickel-based superalloy during tensile at room temperature”, *Materials Science and Engineering: A*, vol. 744, pp. 154–162, Jan. 2019.

[15] J. Zhang, T. Murakumo, H. Harada, Y. Koizumi, and T. Kobayashi, “Creep Deformation Mechanisms in Some Modern Single-Crystal Superalloy”, 2004.

[16] M. J. Donachie and S. J. Donachie, *Superalloys: A Technical Guide, Second Edition*. ASM International, 2002.

[17] R. C. Reed, E. S. Huron, and M. C. Hardy, Eds., *Superalloys 2012*. Wiley & Sons, In., 2012.

[18] K. Park and P. Withey, “Compositions of Gamma and Gamma Prime Phases in an As-Cast Nickel-Based Single Crystal Superalloy Turbine Blade”, *Crystals (Basel)*, vol. 12, no. 2, Feb. 2022.

[19] F. Masoumi, D. Shahriari, M. Jahazi, J. Cormier, and A. Devaux, “Kinetics and Mechanisms of γ′ Reprecipitation in a Ni-based Superalloy”, *Scientific Reports*, vol. 6, Jun. 2016.

[20] R. A. Ricks, A. J. Porter, and R. C. Ecob, “The Growth Of γ’ Precipitates Superalloys in Nickel-Base Superalloys”, 1983.

[21] X. He, J. Zhang, Y. Peng, J. Li, J. Ding, C. Liu, X. Xia, X. Chen, Y. Liu, “Microstructure Evolution of Primary γ′ Phase in Ni3Al-Based Superalloy”, *Acta Metallurgica Sinica*, vol. 33, no. 12, pp. 1709–1726, Dec. 2020.

[22] A. Devaux, L.Naz, R. Molins, A. Pineau, A. Organista, J.Y. Guedou, J. F. Uginet, P. Heritier, “Gamma double prime precipitation kinetic in Alloy 718”, *Materials Science and Engineering: A*, vol. 486, no. 1–2, pp. 117–122, Jul. 2008.

[23] X. Z. Qin, J. T. Guo, C. Yuan, J. S. Hou, and H. Q. Ye, “Precipitation and thermal instability of M23C6 carbide in cast Ni-base superalloy K452”, *Materials Letters*, vol. 62, no. 2, pp. 258–261, Jan. 2008.

[24] L. M. Pike, “Development of A Fabricable Gamma-Prime Strengthened Superalloy”, 2008.

[25] H. E. Collins, “Relative Stability of Carbide and Intermetallic Phases in Nickel-Base Superalloys”, 1969.

[26] H. Matysiak, M. Zagorska, J. Andersson, A. Balkowiec, R. Cygan, M. Rasinski, M. Pisarek, M. Andrzejczuk, K. Kubiak, K. J. Kurzydlowski, “Microstructure of Haynes® 282® superalloy after vacuum induction melting and investment casting of thin-walled components”, *Materials*, vol. 6, no. 11, pp. 5016–5037, 2013.

[27] S. Singh Handa, “Precipitation of Carbides in a Ni-based Superalloy.” University West, 2014.

[28] T. Sugui, W. Minggang, L. Tang, Q. Benjiang, and X. Jun, “Influence of TCP phase and its morphology on creep properties of single crystal nickel-based superalloys”, *Materials Science and Engineering: A*, vol. 527, no. 21–22, pp. 5444–5451, 2010.

[29] J. Zhang, F. Lu, and L. Li, “An Overview of Thermal Exposure on Microstructural Degradation and Mechanical Properties in Ni-Based Single Crystal Superalloys”, *Materials*, vol. 16, no. 5. MDPI, Mar. 01, 2023.

[30] M. C. Hardy, M. Detrois, E. T. Mcdevitt, C. Argyrakis, V. Saraf, P. D. Jablonski, J. A. Hawk, R. C. Buckingham, H. S. Kitaguchi, S. Tin., “Solving Recent Challenges for Wrought Ni-Base Superalloys”, *Metallurgical and Materials Transactions 50th Anniversary Collection*, vol. 51, no. 6, pp. 2626–2650, Jun. 2020.

[31] Wangyao P, Krongtong V, Homkrajai W, Polsilapa S, and Lothongkum G, “Comparing Rejuvenated Microstructures After Hip Process and Different Heat Treatments in Cast Nickel Base Superalloys, In-738 And Gtd-111 After Long-Term Service”, 2006.

[32] S. Farahany, M. Aghaie-Khafri, A. Ourdjini, and M. H. Idris, “Influence of heat treatment on properties of hot isostatically pressed turbine blade superalloy IN738”, *Advanced Materials Research*, pp. 502–507, 2011.

[33] H. Colleen, A. Wessman, R. Aman, M. Eff, R. Hayes, B. Dimarco, E. Herderik, W. Zhang, M. Mills, “Effect of Solutionizing Heat Treatment on Microstructure and Mechanical Behavior of Additively Manufactured Medium Gamma Prime Nickel Superalloy”, *Metallurgical and Materials Transactions 50th Anniversary Collection*, vol. 54, no. 6, pp. 2470–2485, Jun. 2023.

[34] S. R. Hegde, R. M. Kearsey, and J. Beddoes, “Design of Solutionizing Heat Treatments for an Experimental Single Crystal Superalloys”, 2008.

[35] R. C. Kramb, M. M. Antony, and S. L. Semiatin, “Homogenization of a nickel-base superalloy ingot material”, *Scripta Materiala*, vol. 54, no. 9, pp. 1645–1649, May 2006.

[36] Y. Guan, Y. Liu, Z. Ma, H. Li, and H. Yu, “Precipitation and coarsening behavior of γ′ phase in CoNi-base superalloy under different aging treatments”, *Vacuum*, vol. 175, May 2020.

[37] Z. Feng, Z. Wen, M. Li, Y. Zhao, and Z. Yue, “Effect of aging heat treatment on microstructure of Ni-based single crystal superalloys”, *AIP Advances*, vol. 11, no. 12, Dec. 2021.

[38] S. Gorgannejad, E. A. Estrada Rodas, and R. W. Neu, “Ageing kinetics of Ni-base superalloys”, *Materials at High Temperatures*, vol. 33, no. 4–5, pp. 291–300, Jun. 2016.

[39] M. Yang, J. Zhanga, H. Wei, W. Gui, H. Su, T. Jin, L. Liu, “Influence of cooling rate on the formation of bimodal microstructures in nickel-base superalloys during continuous two-step aging”, *Computational Materials Science*, vol. 149, pp. 14–20, Jun. 2018.

[40] G. Cacciamani, “An Introduction to the Calphad Method and the Compound Energy Formalism (Cef)”, *Tecnologia em Metalurgia Materiais e Mineracão*, vol. 13, no. 1, pp. 16–24, 2016.

[41] N. Saunders, M. Fahrmann, and C. J. Small, “The Application of Calphad Calculations to Ni-Based Superalloys”, *The Minerals, Metals and Materials Society*, pp. 803–811, August. 2012.

[42] J. Ågren, “Calculation of phase diagrams: Calphad”, *Current Opinion in Solid State and Materials Science*, vol. 1, no. 3, pp. 355–360, 1996.

[43] U. R. Kattner, “The Calphad Method and Its Role in Material and Process Development”, *Tecnologia em Metalurgia Materiais e Mineracão*, vol. 13, no. 1, pp. 3–15, 2016.

[44] X. Zhuang, S. Lu, L. Li, and Q. Feng, “Microstructures and properties of a novel γ′-strengthened multi-component CoNi-based wrought superalloy designed by CALPHAD method”, *Materials Science and Engineering: A,* vol. 780, Apr. 2020.

[45] E. Rogoff, M. Antony, and P. Markle, “Calculating Ti-6Al-4V β Transus Through a Chemistry-Based Equation Derived from Combined Element Binary

Phase Diagrams", *Journal of Materials Engineering and Performance*, vol. 27, no. 10, pp. 5227–5235, Oct. 2018.

[46] D. S. Gandel, M. A. Easton, M. A. Gibson, and N. Birbilis, "CALPHAD simulation of the Mg-(Mn, Zr)-Fe system and experimental comparison with as-cast alloy microstructures as relevant to impurity driven corrosion of Mg-alloys", *Materials Chemistry and Physics*, vol. 143, no. 3, pp. 1082–1091, Feb. 2014.

[47] R. Wagner, R. Kampmann, and P. W. Voorhees, "Homogeneous Second-Phase Precipitation", 1986.

[48] J. Svoboda, F. D. Fischer, P. Fratzl, and E. Kozeschnik, "Modelling of kinetics in multi-component multi-phase systems with spherical precipitates I: Theory", *Materials Science and Engineering: A*, vol. 385, no. 1–2, pp. 166–174, Nov. 2004.

[49] J. Svoboda, F. D. Fischer, and P. H. Mayrhofer, "A model for evolution of shape changing precipitates in multicomponent systems", *Acta Materiala*, vol. 56, no. 17, pp. 4896–4904, Oct. 2008.

[50] J. E. Morral and G. R. Purdy, "The Calphad Method and Its Role in Material And Process Development", 1994.

[51] E. Kozeschnik, J. Svoboda, P. Fratzl, and F. D. Fischer, "Modelling of kinetics in multi-component multi-phase systems with spherical precipitates II: Numerical solution and application", *Materials Science and Engineering: A*, vol. 385, no. 1–2, pp. 157–165, Nov. 2004.

[52] F. R. N. Nabarro, "The Strains Produced by Precipitation in Alloys", 1940.

[53] S. F. Medina, "From Heterogeneous to Homogeneous Nucleation for Precipitation in Austenite Of Micro alloyed Steels", 2015.

[54] "Precipitation Nucleation." Available: https://computherm.com/Pandat_OnlineHelp/Content/5-PanPrecipitation/1_Features %20of%20PanPrecipitation/3.1_PrecipitateNucleat.htm

[55] A. E. Nielsen, “Supersaturated Solution”, 1970.

[56] C. Llc, “PandatTM 2023 User’s Guide”, 2000.

[57] M. Perez, “Gibbs-Thomson effects in phase transformations”, *Scripta Materiala*, vol. 52, no. 8, pp. 709–712, 2005.

[58] T. Zhou, P. Hedstr̲m, D. San Martin, “Integrated Experimental and Computational Study of Precipitation in Martensitic Steels”, KTH Royal Institute of Technology, 2019.

[59] M. J. Anderson, C. Panwisawas, Y. Sovani, R. P. Turner, J. W. Brooks, and H. C. Basoalto, “Mean-field modelling of the intermetallic precipitate phases during heat treatment and additive manufacture of Inconel 718”, *Acta Materiala*, vol. 156, pp. 432–445, Sep. 2018.

[60] E. Kozeschnik, J. Svoboda, and F. D. Fischer, “Shape factors in modeling of precipitation”, *Materials Science and Engineering: A*, vol. 441, no. 1–2, pp. 68–72, Dec. 2006.

[61] H. Wendt and P. Haasen, “Nucleation and Growth Of F-Precipitates In Ni-14 At.% Al”, 1983.

[62] Z. Sheng, M. Bonvalet Rolland, T. Zhou, J. Odqvist, and P. Hedström, “Langer–Schwartz–Kampmann–Wagner precipitation simulations: assessment of models and materials design application for Cu precipitation in PH stainless steels”, *Journal of Materials Science*, vol. 56, no. 3, pp. 2650–2671, Jan. 2021.

[63] C. Sommitsch, E. Kozeschnik, G. Wasle, and B. Buchmayr, “A Precipitation Model for Multi-Component Multi-Phase Systems in Nickel-Base Superalloys”, 2000.

[64] Y. H. Wen, B. Wang, J. P. Simmons, and Y. Wang, “A phase-field model for heat treatment applications in Ni-based alloys”, *Acta Materiala*, vol. 54, no. 8, pp. 2087–2099, May 2006.

[65] K. Zhang, F. Yu, M. Zhu, J. Dan, X. Wang, J. Zhang, B. Dai, “Enhanced low temperature NO reduction performance via MnOx-Fe2O3/vermiculite monolithic honeycomb catalysts”, *Catalysts*, vol. 8, no. 3, Mar. 2018.

[66] M. Bonvalet, T. Philippe, X. Sauvage, and D. Blavette, “Modeling of precipitation kinetics in multicomponent systems: Application to model superalloys”, *Acta Materiala*, vol. 100, pp. 169–177, Nov. 2015.

[67] R. Wagner, R. Kampmann, and P. W. Voorhees, “Homogeneous Second-Phase Precipitation”, 1986

[68] A. J. Ardell, “Precipitation Hardening”, 1985.

[69] L. Brown and R. Ham, “Dislocaton-particle interactions in Kelly, A and Nicholson, RB.”, *Strengthening methods in crystals*, J. Wiley and Sons, 1971.

[70] A. Kelly and K. B. Nicholson, “Precipitation hardening”, *Progress in Materials Science*, vol. 10, Macmillan, 1963.

[71] R. Watana Be and T. Kuno, “Alloy Design of Nickel-base Precipitation Hardened Superalloys”, 1975.

[72] D. J. Wilson, “Deformation Characteristics and Time-Dependent Notch Sensitivity of Udimet 700 at Intermediate Temperatures Final Report”, 1974.

[73] A. Takahashi, M. Kawanabe, and N. M. Ghoniem, “γ-precipitate strengthening in nickel-based superalloys”, *Philosophical Magazine*, pp. 3767–3786, Sep. 2010.

[74] K. Owusu-Boahen, M. Bamberger, S. F. Dirnfeld, B. Prinz, and J. Klodt, “Precipitation hardening in nicl<el based superalloys: effect of alloying”, 1996.

[75] W. Li, J. Ma, H. Kou, J. Shao, X. Zhang, Y. Deng,Y. Tao, D. Fang, “Modeling the effect of temperature on the yield strength of precipitation strengthening Ni-base superalloys”, *International Journal of Plasticity*, vol. 116, pp. 143–158, May 2019.

[76] J. Zang, “Creep of Second Phase Particles Strengthened Materials”, *High Temperature Deformation and Fracture of Materials*, 2007.

[77] J. P. Hirth, R. W. Cahn, and P. Haasent, “Dislocations”, *Physical Metallurgy*, 1996.

[78] A. J. Goodfellow, E. I. Galindo-Nava, C. Schwalbe, and H. J. Stone, “The role of composition on the extent of individual strengthening mechanisms in polycrystalline Ni-based superalloys”, *Materials and Design*, vol. 173, Jul. 2019.

[79] R. W. Kozar, A. Suzuki, W. W. Milligan, J. J. Schirra, M. F. Savage, and T. M. Pollock, “Strengthening mechanisms in polycrystalline multimodal nickel-base superalloys”, *Metallurgical and Materials Transactions A: Physical Metallurgy and Materials Science*, vol. 40, no. 7, pp. 1588–1603, 2009.

[80] T. Zhou, P. Hedstrm, D. San Martin, “Integrated Experimental and Computational Study of Precipitation in Martensitic Steels”, KTH Royal Institute of Technology, 2019.

[81] H. Wen, T. D. Topping, D. Isheim, D. N. Seidman, and E. J. Lavernia, “Strengthening mechanisms in a high-strength bulk nanostructured Cu-Zn-Al alloy processed via cryomilling and spark plasma sintering”, *Acta Materiala*, vol. 61, no. 8, pp. 2769–2782, May 2013.

[82] V. Gehold and H. Habehkorn, “On the Critical Resolved Shear Stress by of Solid Solutions Containing Coherent Precipitates”, 1966.

[83] W. Li, J. Ma, H. Kou, J. Shao, X. Zhang, Y. Deng,Y. Tao, D. Fang, “Modeling the effect of temperature on the yield strength of precipitation strengthening Ni-base superalloys”, *International Journal of Plasticity*, vol. 116, pp. 143–158, May 2019.

[84] J. M. Oblak, D. F. Paulonis, D. S. Duvall, and D. S. Duvall Senior, “Coherency Strengthening in Ni Base Alloys Hardened by D022 Precipitates”, 1974.

[85] A. Kelly and R. B. Nicholson, *Strengthening methods in crystals*, no. 4. Elsevier BV, 1971.

[86] E. J. Mittemeijer, "Fundamentals of Materials Science: The Microstructure Property Relationship Using Metals as Model Systems", 2010.

[87] R. W. Hertzberg, *Deformation and Fracture Mechanics of Engineering Materials*, 4th edition. Wiley and Sons Inc, 1996.

[88] F. Czerwinski, F. Samuel, A. Mohamed, and F. Samuel, "A review on the heat treatment of Al-Si-Cu/Mg casting alloys", *Heat Treatment-Conventional and Novel Applications*, 2012.

[89] A. Argon, *Strengthening Mechanisms in Crystal Plasticity*, Oxford University Press, 2007.

[90] R. W. Cahn and P. Haasen, *Physical Metallurgy*, 4th edition. North Holland, 1996.

[91] R. L. Fleischert, "Substitutional Solution Hardening", 1963.

[92] G. E. Dieter, *Mechanical Metallurgy*, 1988.

[93] M. Al-saadi, F. Sandberg, P. G. Jönsson, and C. N. Hulme-smith, "Modelling of strengthening mechanisms in wrought nickel-based 825 alloy subjected to solution annealing", *Metals (Basel)*, vol. 11, no. 5, 2021.

[94] Y. Mishima, S. Ochiai, N. Hamao, M. Yodogawa, and T. Suzuki, "Solid Solution Hardening of Nickel-Role of Transition Metal and B-subgroup Solutes", 1986.

[95] E. I. Galindo-Nava, L. D. Connor, and C. M. F. Rae, "On the prediction of the yield stress of unimodal and multimodal γ' Nickel-base superalloys", *Acta Materiala*, vol. 98, pp. 377–390, Aug. 2015.

[96] R. Labusch, "A Statistical Theory of Solid Solution Hardening a Statistical Theory of Solid Solution Hardening", 1970.

[97] A. P. Sutton and R. W. Balluffi, *Interfaces in crystalline materials*, Clarendon Press, 1995.

[98] W. D. Callister and D. G. Retwisch, *Materials Science and Engineering: An Introduction*, 10th edition, Wiley, 2018.

[99] J. Antonio and V. Ortiz, "Preventing solidification defects in large superalloy castings used Preventing solidification defects in large superalloy castings used in advanced electric power systems in advanced electric power systems", 2010.

[100] R. J. Siddall, "Comparison of the Attributes of VIM + ESR and VIM + VAR Alloy 718", *The Minerals, Metals & Materials Society*, 1991.

[101] W.-D. Cao, "US6730264", US 6,730,264 B2, May 04, 2004.

[102] M. A. Neri, A. Martinez -Villafañe, C. Carreño, A. D. Gonzalez Escarcega, O. Cobarrubias-Alvarado, "Metallurgical Characterization of Waspaloy Presenting Variations in Chemical Composition, Grain Size and Hardness", *The Minerals, Metals & Materials Society*, 2012.

[103] O. Lypchanskyi, T. Śleboda, K. Zyguła, A. Łukaszek-Sołek, M. Wojtaszek, "Evaluation of hot workability of nickel-based superalloy using activation energy map and processing maps", *Materials*, vol. 13, no. 16, Aug. 2020.

[104] I. Dempster, W.-D. Cao, R. Kennedy, B. Bond, J. Aurrecoechea, and M. Lipschutz, "Structure and Property Comparison of Allvac ® 718plus Alloy and Waspaloy Forgings", *The Minerals, Metals & Materials Society*, 2005.

[105] A. Chamanfar, "Evolution of Microstructure and Mechanical Properties in Linear Friction Welded Waspaloy", 2012.

[106] B. A. Lerch, N. Jayaraman, and S. D. Antolovich, "A Study of Fatigue Damage Mechanisms in Waspaloy from 25 to 800 °C", 1984.

[107] L. Xue, “Laser Consolidation—A Rapid Manufacturing Process for Making Net-Shape Functional Components”, *Advances in Laser Materials Processing: Technology, Research and Applications*, Elsevier, pp. 461–505, 2017.

[108] J. Andersson, V. Hosseini, M. Neikter, and R. Pederson, “Welding of special alloys”, *Welding of Metallic Materials: Methods, Metallurgy, and Performance*, Elsevier, pp. 279–316, 2023.

[109] G. Liu, X. Xiao, M. Véron, and S. Birosca, “The nucleation and growth of η phase in nickel-based superalloy during long-term thermal exposure”, *Acta Materiala*, vol. 185, pp. 493–506, Feb. 2020.

[110] M. Rahimian, S. Milenkovic, and I. Sabirov, “Microstructure and hardness evolution in MAR-M247 Ni-based superalloy processed by controlled cooling and double heat treatment”, *Journal of Alloys and Compounds*, vol. 550, pp. 339–344, Feb. 2013.

[111] S. Hammadi, “Solidification Modeling of Microsegregation”, 2018.

[112] I. M. Wolff, “Precipitation Accompanying Overheating in Nickel-Base Superalloy”, *Materials Characterization*, 1992.

[113] “Standard Practice for Microetching Metals and Alloys”, ASTM Internationa, 1999.

[114] P. Zhang, S. X. Li, and Z. F. Zhang, “General relationship between strength and hardness”, *Materials Science and Engineering: A*, vol. 529, no. 1, pp. 62–73, 2011.

[115] S. Utada, R. Sasaki, R. C. Reed, and Y. T. Tang, “Overheating of Waspaloy: Effect of cooling rate on flow stress behavior”, *Materials and Design*, vol. 221, Sep. 2022.

[116] D. S. Mackenzie and G. E. Totten, *Analytical Characterization of Aluminum, Steel, And Superalloys*, CRC Press, 2006.

[117] Y. Y. Zhao and T. G. Nieh, “Correlation between lattice distortion and friction stress in Ni-based equiatomic alloys”, *Intermetallics (Barking)*, vol. 86, pp. 45–50, Jul. 2017.

[118] H. Bhadeshia and R. Honeycombe, *Steels - Microstructure and Properties*, 3rd ed. Elsevier, 2006.

[119] G. E. Maurer, L. A. Jackman, and J. A. Domingue, “Role of Cobalt In Waspaloy”, 1980.

[120] R. L. Dreshfield and J. F. Wallace, “The Effect of Alloying On Gamma And Gamma Prime In Nickel-Base Superalloys”, 1972.

[121] S. Kumar K.G.V. and R. A. Gerhardt, “Effect of high temperature exposure on the microstructure of Waspaloy”, *Microscopy and Microanalysis*, pp. 688–689, 2004.

[122] M. V Nathal, R. A. Mackay, and R. G. Garlick, “Temperature Dependence of ɣ/ɣ' Lattice Mismatch in Nickel-base Superalloys”, 1985.

[123] R. F. Decker, A. I. Rush, A. G. Dano, J. W. Freeman, “Abnormal Grain Growth in Nickel-Base Heat Resistant Alloys”, 1956.

[124] J. Moravec, “Determination of the grain growth kinetics as a base parameter for numerical simulation demand”, *MM Science Journal*, vol. 2015, pp. 649–653, Oct. 2015.

[125] M. A. Neri, A. Martinez -Villafañe, C. Carreño, A. D. Gonzalez Escarcega, O. Cobarrubias-Alvarado, “Metallurgical Characterization of Waspaloy Presenting Variations in Chemical Composition, Grain Size and Hardness”, *The Minerals, Metals & Materials Society*, 2012.

[126] E. N. Borodin, A. A. Gruzdkov, A. E. Mayer, and N. S. Selyutina, “Physical nature of strain rate sensitivity of metals and alloys at high strain rates”, *Journal of Physics: Conference Series*, Institute of Physics Publishing, Apr. 2018.

[127] L. Wang, Y. Liu, X. Song, J. Jin, J. Du, and B. Zhang, “Study on The Strain Rate Sensitivity of A Ni-Based Superalloy”, *The Minerals, Metals & Materials Society*, 2013.

APPENDICES

A. XRD diffraction peak of heat-treated Waspaloy at 850°C for 18-hours.

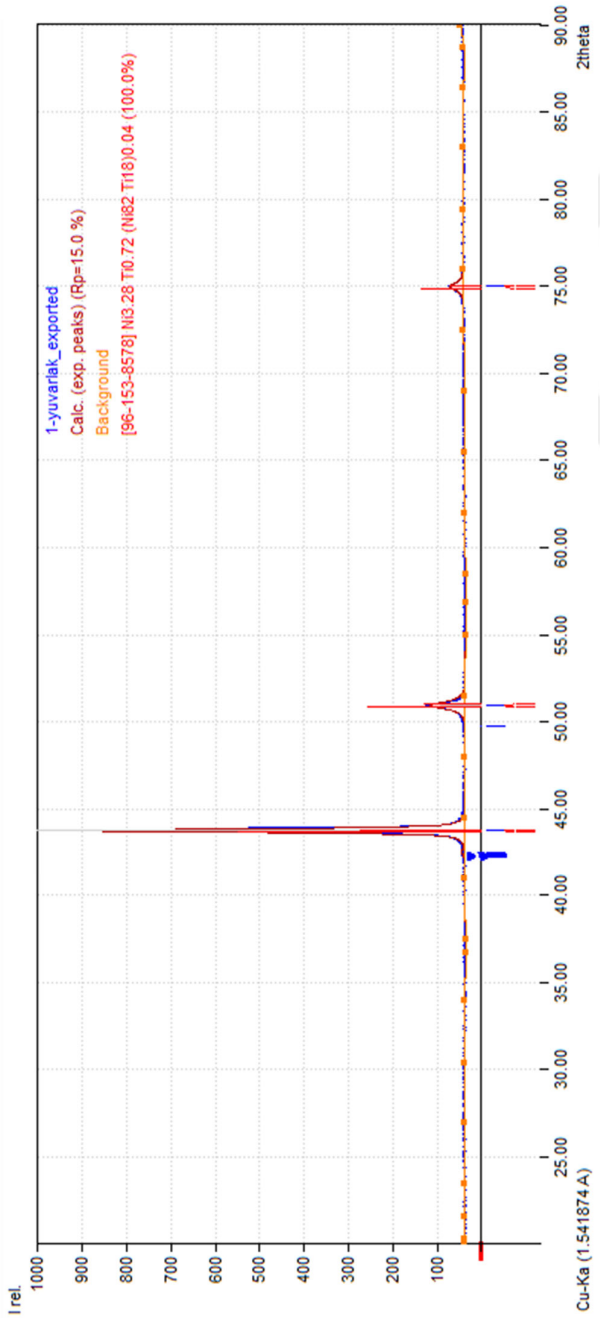

B. Oxygen diffusion analysis for ɣ-matrix through solutionizing and aging.

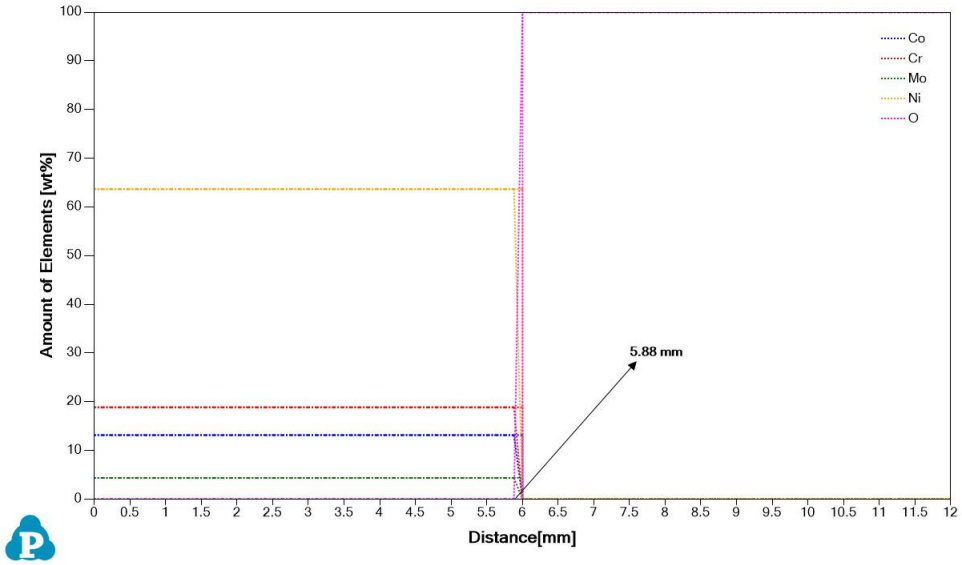

C. Lattice strength of pure Nickel with temperature obtained with JMatPro.

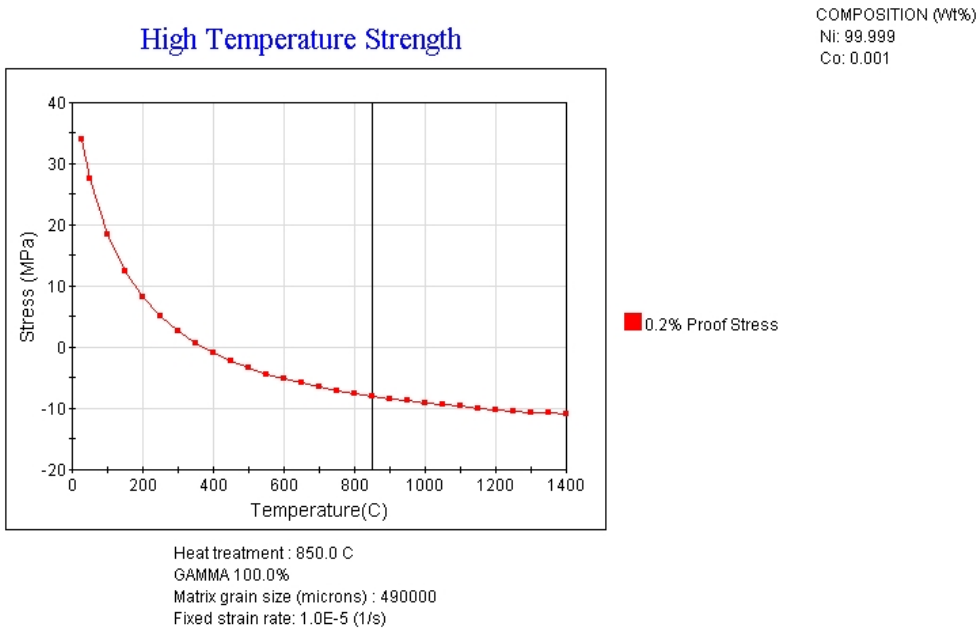

D. Poisson's ratio of Waspaloy with temperature obtained with JMatPro.

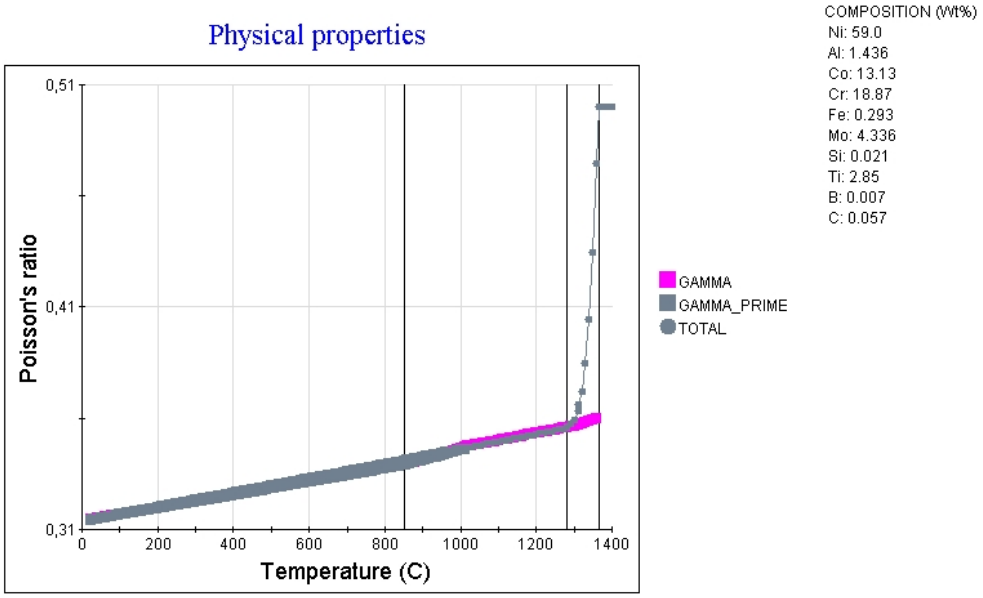

E. Shear modulus of Waspaloy with temperature obtained with JMatPro.

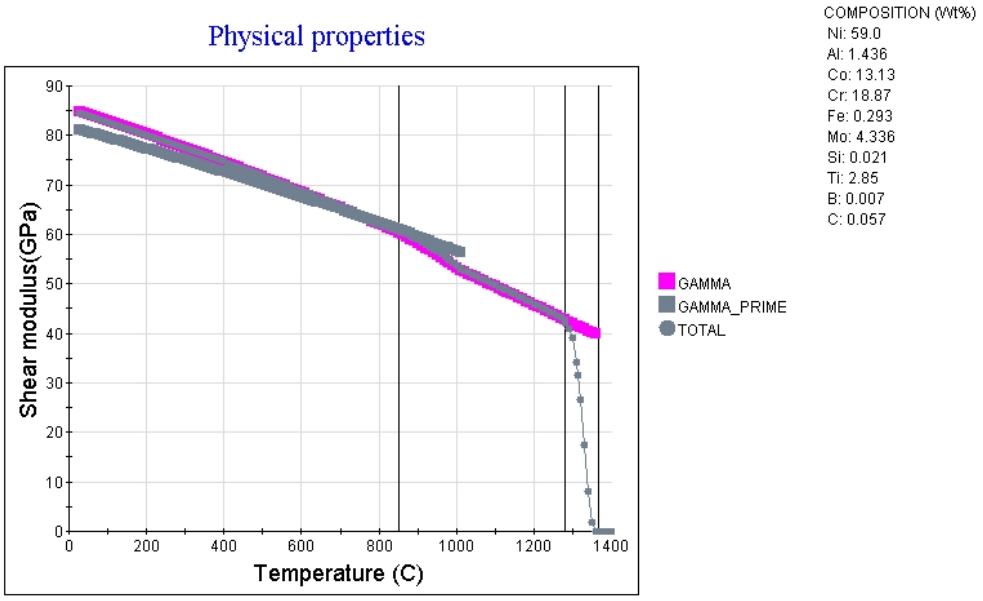

F. Lattice parameter of ɣ and ɣ' with temperature obtained with JMatPro.

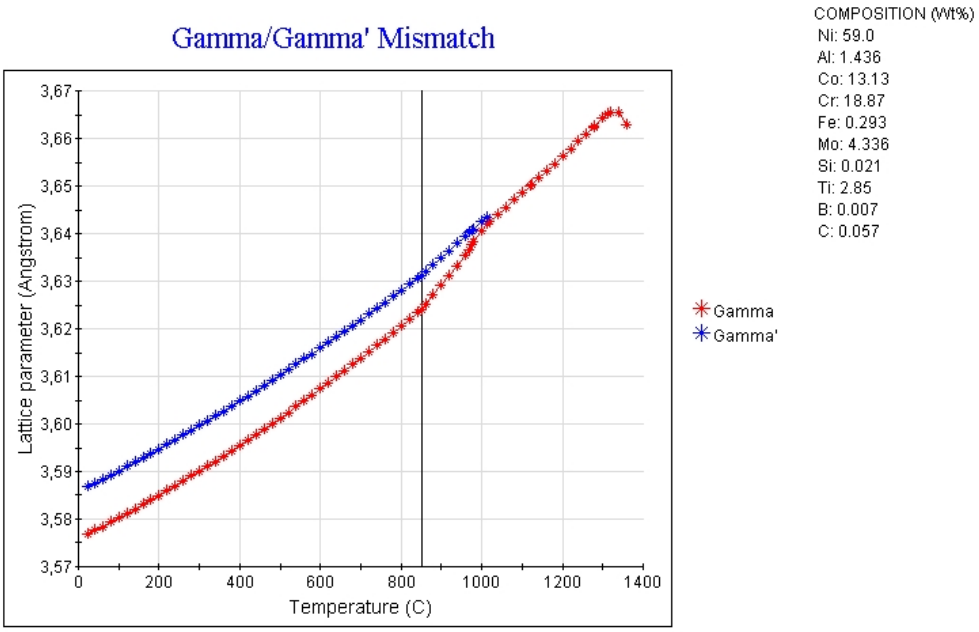

G. Yield strength estimation of PANDAT software through aging.

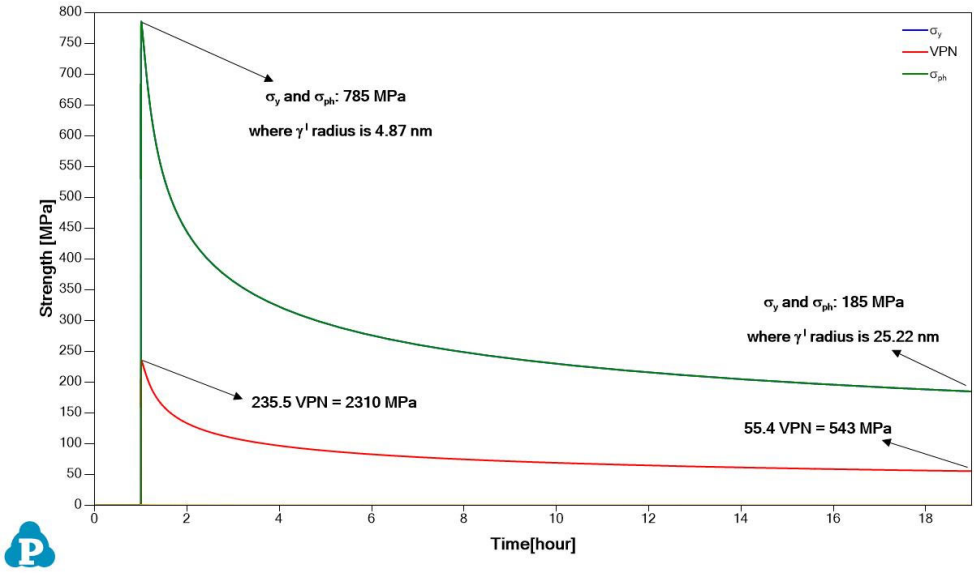

H. SMR 311 Tensile Test Specimen Geometry for Gleeble 3500 system.

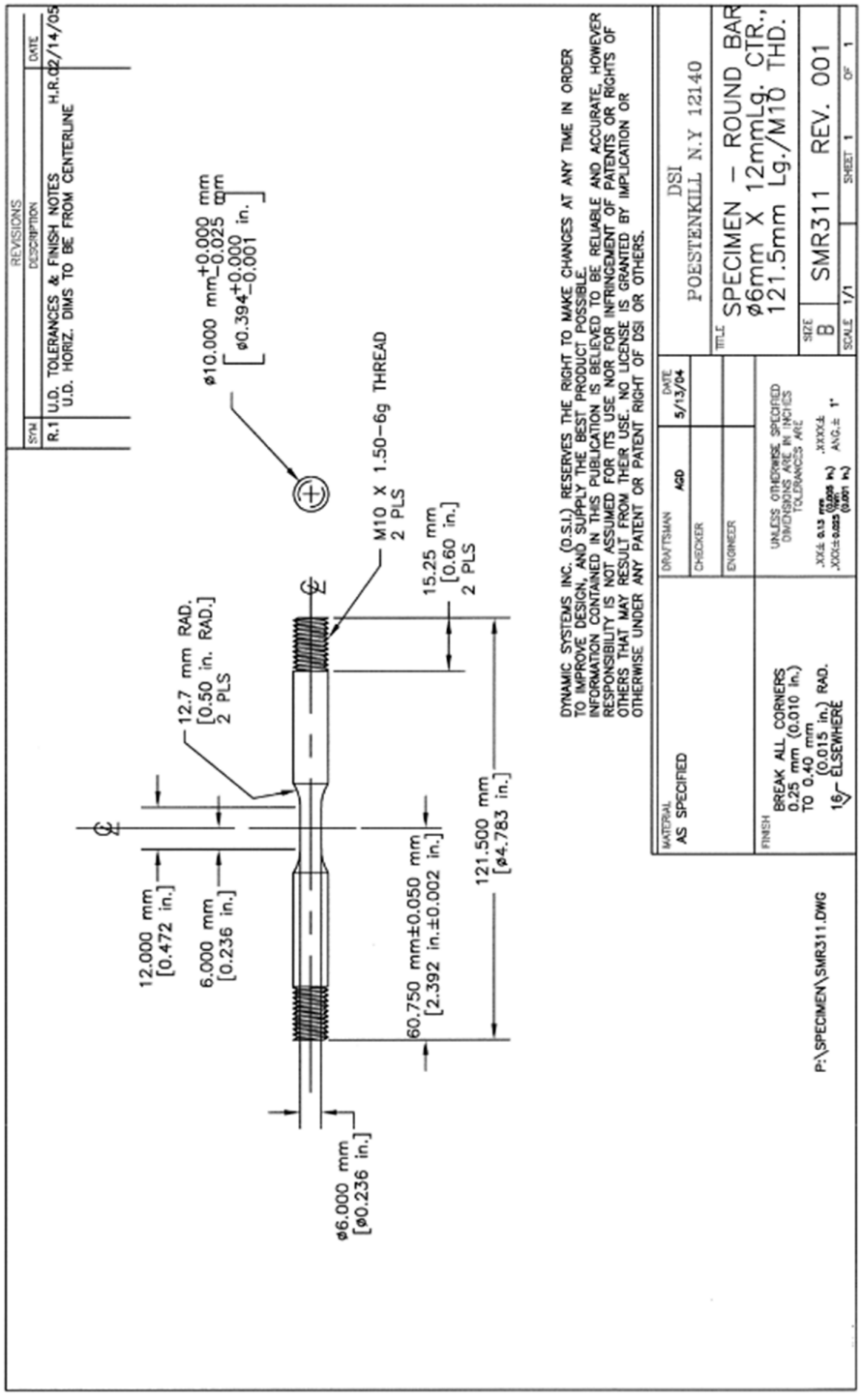

I. Yield strength experiment results completed with Gleeble 3500.

Test Condition	Mean UTS [MPa]	Standard Deviation in Ultimate Tensile Strength [MPa]	Mean σ_y [MPa]	Standard Deviation in Yield Strength [MPa]
RT – 0.001SR	1538.2	372.7	777.8	49.4
RT – 1SR	1780.9	70.4	792.4	6.2
580°C – 0.001SR	1270.9	114.6	656.6	4.8
580°C – 1SR	1316.7	38.1	673.9	47.1
650°C – 0.001SR	1404.5	261.6	658.9	13.5
650°C – 1SR	1448.6	20.6	665.7	17.5
720°C – 0.001SR	1073.5	19.4	619.3	29.7
720°C – 1SR	1244.1	7.3	674.1	4.1
1000°C – 0.001SR	68.5	-	53.1	4.7
1000°C – 0.01SR	103.2	15.2	94.8	1.5
1000°C – 0.1SR	164.7	21.8	138.3	4.3
1000°C – 1SR	231.7	9.5	187.9	3.4